The Astrophysical Journal, 979:170 (31pp), 2025 February 1 https://doi.org/10.3847/1538-4357/ad9c64

Hydrogen Column Density Variability in a Sample of Local Compton-thin AGN II

A. Pizzetti[1,2,9,11], N. Torres-Albà[2,3,10], S. Marchesi[2,4,5], J. Buchner[6], I. Cox[2], X. Zhao[7], S. Neal[2], D. Sengupta[4,5], R. Silver[8], and M. Ajello[2]
[1] European Southern Observatory, Alonso de Córdova 3107, Casilla 19, Santiago 19001, Chile
[2] Department of Physics and Astronomy, Clemson University, Kinard Laboratory of Physics, Clemson, SC 29634, USA
[3] Department of Astronomy, University of Virginia, P.O. Box 400325, Charlottesville, VA 22904, USA
[4] Dipartimento di Fisica e Astronomia (DIFA), Università di Bologna, via Gobetti 93/2, I-40129 Bologna, Italy
[5] INAF—Osservatorio di Astrofisica e Scienza dello Spazio di Bologna, Via Piero Gobetti, 93/3, 40129, Bologna, Italy
[6] Max-Planck-Institut für extraterrestrische Physik, Giessenbachstraße 1, D-85748 Garching, Germany
[7] Department of Astronomy, University of Illinois at Urbana-Champaign, Urbana, IL 61801, USA
[8] NASA Goddard Space Flight Center, Greenbelt, MD 20771, USA
Received 2024 March 8; revised 2024 October 14; accepted 2024 November 25; published 2025 January 24

Abstract

We present the multiepoch analysis of 13 variable, nearby ($z \lesssim 0.1$), and Compton-thin ($10^{22} < N_{\rm H} < 1.5 \times 10^{24}\,{\rm cm}^{-2}$) active galactic nuclei (AGN) selected from the 105-month BAT catalog. Analyzing all available archival soft and hard X-ray observations, we investigate the line-of-sight hydrogen column density ($N_{\rm H,los}$) variability on timescales ranging from a few days to approximately 20 yr. Each source is analyzed by simultaneously modeling the data with three physical torus models, providing tight constraints on torus properties, including the covering factor, the cloud dispersion, and the torus average hydrogen column density ($N_{\rm H,av}$). Our final sample includes 27 variable, Compton-thin AGN after implementing another 14 AGN analyzed in our previous work. We find that all sources require either flux or $N_{\rm H,los}$ variability. Based on the degree of variability, we classify 37% of them as "$N_{\rm H,los}$ Variable," 44% as "Nonvariable in $N_{\rm H,los}$," and 19% as "Undetermined." Noticeably, there is no discernible difference between geometrical and intrinsic properties among the three variability classes, suggesting no intrinsic differences between the $N_{\rm H,los}$-variable and nonvariable sources within the considered sample. We measure the median variation in $N_{\rm H,los}$ between any observation pair of the same source to be 25% with respect to the lowest $N_{\rm H,los}$ measure in the pair. Furthermore, 48% of the analyzed sources require the inclusion of a Compton-thick reflector in the spectral fitting. Among these, 30% exhibit recorded 22 GHz water megamaser emission, suggesting a potential shared nature between the two structures.

Unified Astronomy Thesaurus concepts: Active galactic nuclei (16); Active galaxies (17); High energy astrophysics (739); X-ray active galactic nuclei (2035)

1. Introduction

Active Galactic Nuclei (AGN) are among the brightest and most energetic objects in the Universe. They are powered by a supermassive black hole (SMBH) at the center of the host galaxy, accreting matter from an accretion disk surrounded by a toroidal structure of gas and dust, which is the obscuring torus (R. Antonucci 1993; C. M. Urry & P. Padovani 1995). Ultraviolet photons arising from the accretion disk get up-scattered to X-rays via inverse Compton scattering by hot electrons close to the accretion disk (F. Haardt et al. 1994; C. Ramos Almeida & C. Ricci 2017; V. E. Gianolli et al. 2023). Because they are produced in the very center of the AGN, X-ray photons are powerful messengers that probe the physics of the accretion system and the matter in its surroundings. Although recent studies (see, e.g., J. Buchner & F. E. Bauer 2017; C. Andonie et al. 2022) have shown a minor part of the obscuration to be generated on galactic scales, submillimeter, infrared, optical and X-ray studies (see, e.g., G. Risaliti et al. 2002, 2005; C. Simpson 2005; K. D. Murphy & T. Yaqoob 2009; S. Furui et al. 2016; F. Combes et al. 2019; S. F. Hönig 2019; S. Garcìa-Burillo et al. 2021, and references therein) infer the presence of a torus-like structure of molecular and atomic gas and dust on parsec scales as the origin of the obscuration and reprocessing of the incoming AGN radiation.

The atomic and molecular gas density in the torus is typically parameterized in X-rays as the line-of-sight neutral hydrogen column density $N_{\rm H,los}$. When the X-ray-obscuring matter has a column density which is equal to or larger than the inverse of the Thomson cross-section $\sigma_{\rm T}$, $N_{\rm H,los} \geqslant \sigma_{\rm T}^{-1} \simeq 1.5 \times 10^{24}\,{\rm cm}^{-2}$, the source is defined as Compton-thick (CT) AGN (e.g., R. R. Ross 1979; A. Comastri 2004), and we define it as obscured Compton-thin when $10^{22}\,{\rm cm}^{-2} < N_{\rm H,los} < 1.5 \times 10^{24}\,{\rm cm}^{-2}$. Despite the presence of other spectral components, such as thermal emission from hot plasma in the host galaxy (e.g., A. Comastri 2004; N. Torres-Albà et al. 2018), the 2–10 keV X-ray spectrum of obscured AGN is characterized by the photoabsorption of the main power-law photons by the gas in the line of sight (the so-called *transmitted component* of the X-ray spectrum). Infrared and X-ray analyses (e.g., G. Risaliti et al. 2002, 2005; S. Bianchi et al. 2005; M. Schartmann et al. 2005; G. Risaliti et al. 2007; M. Nenkova et al. 2008a, 2008b; M. Sanfrutos et al. 2013; A. G. Markowitz et al. 2014; S. Laha et al. 2020; J. Buchner et al. 2021) have ruled out the initial idea of a homogeneous torus, favoring a clumpy scenario in which the torus is a structure of

[9] ESO Fellow.
[10] GECO Fellow.
[11] Corresponding author.

moving clouds of different densities, embedded in a less dense, intercloud medium. Indeed, recent studies have shown how the X-ray obscuration is likely to be produced by multiple absorbers on various spatial scales (C. Ramos Almeida & C. Ricci 2017; J. Buchner et al. 2019; S. Marchesi et al. 2022; A. Pizzetti et al. 2022; R. Serafinelli et al. 2023; N. Torres-Albà et al. 2023), matching the description of an obscurer with a complex structure made of clouds with different column densities. In addition, $N_{\rm H,los}$ variability studies on large source samples (e.g., A. G. Markowitz et al. 2014; L. Hernández-Garcìa et al. 2015; S. Laha et al. 2020) detect only a few sources to be variable, suggesting a scenario in which a more intricate system of clouds of different sizes, densities, and radial velocity is preferred over a simple patchy torus. The modeling of the AGN broadband X-ray spectra and its variability between multiple epochs is thus crucial in revealing precious information about the density and the location of the absorbing media surrounding the central engine and how it connects with the large-scale structures of the host galaxies (see, e.g., G. Risaliti et al. 2005; M. Baloković et al. 2018; S. Marchesi et al. 2022; A. Pizzetti et al. 2022; N. Torres-Albà et al. 2023).

In this work, we present the multiepoch X-ray analysis of a sample of 13 potentially $N_{\rm H,los}$ variable obscured AGN, each of which has multiple X-ray observations covering both the hard and the soft regions of the X-ray spectrum. In most cases, observations are taken over a period of ~20 yr. The spectral analysis is performed by simultaneously fitting all the X-ray spectra available for each source; this approach has proven to be a powerful tool to constrain overall torus parameters that are not expected to change in the considered timescales (e.g., the covering factor, the torus inclination angle, and the torus average column density), while allowing the estimation of $N_{\rm H,los}$ variability, as shown by M. Baloković et al. (2018) and S. Marchesi et al. (2022). In order to have a larger statistical sample, we include in the analysis the sample studied by N. Torres-Albà et al. (2023), as well as NGC 6300 (D. Sengupta et al. 2024) and NGC 7479 (A. Pizzetti et al. 2022). The overall properties of the whole sample of galaxies are thus presented.

This paper is structured as follows: in Sections 2 and 3, we describe the sample selection, the data reduction, and the X-ray spectral analysis processes. We outline the methods used to classify the sources as "Variable," "Nonvariable," and "Undetermined" in Section 4 and in Section 5, we present the obtained results. The computation of the equatorial column densities for `UXCLUMPY` is presented in Section 5.1. We discuss the results obtained from the variability analysis performed on the full sample of galaxies in Section 5.2, and we report our conclusions in Section 6. Information about the best-fit parameters, spectra, $N_{\rm H,los}$-variability plots, and comments on each individual source are presented in Appendices A, B, C, and D, respectively.

The cosmological parameters assumed in this work are compatible with a flat ΛCDM cosmology with $H_0 = 69.6\,{\rm km\,s^{-1}\,Mpc^{-1}}$, $\Omega_m = 0.29$ and $\Omega_\Lambda = 0.71$ (C. L. Bennett et al. 2014). All reported uncertainties are at a 90% confidence level unless otherwise stated.

2. Sample Selection

The sample analyzed in this work is complementary to the one analyzed in N. Torres-Albà et al. (2023; NTA23, hereafter). Both samples have been selected from the work of X. Zhao et al. (2021; XZ21, hereafter), which analyzed 93 Compton-thin AGN with $N_{\rm H,los}$ between 10^{23} and $10^{24}\,{\rm cm^{-2}}$, selected from the 105-month Burst Alert Telescope (BAT; S. D. Barthelmy et al. 2005)—catalog (K. Oh et al. 2018). All the sources analyzed in XZ21 were fitted with at least one NuSTAR observation and one soft X-ray observation, either from XMM-Newton, Chandra, or Swift-XRT. This guarantees low and high-energy X-ray coverage, which is necessary to disentangle the degeneracy between reflection and line-of-sight components.

Of the 93 sources, 22 had simultaneous NuSTAR and soft X-ray observations, and 13 were analyzed using Swift-XRT, which typically exhibits a very low signal-to-noise ratio. In 31 of the remaining 58 sources, XZ21 detected either intrinsic flux or $N_{\rm H,los}$ variability, determined via simultaneous X-ray spectral analysis of one NuSTAR and one soft X-ray observation for each source. We note that in this preliminary analysis by XZ21, for each source, both $N_{\rm H,los}$ and intrinsic flux variability were considered in order to obtain a good fit. Considering that the $N_{\rm H,los}$ and flux variability can be highly degenerate, performing a simultaneous multiepoch analysis of all the observations available for each of the 31 sources is pivotal to better understand the origin of variability, as shown by A. Pizzetti et al. (2022), S. Marchesi et al. (2022), and NTA23. Out of the 31 variable galaxies, NGC 7479 has been analyzed in a pilot project by A. Pizzetti et al. (2022), 12 have been analyzed in NTA23, and two are being excluded due to the lack of new available data with respect to the one analyzed by XZ21 (ESO 201-IG004 and 4C+73.08); NGC 6300, MRK 477, and NGC 7582 are being analyzed in single-source projects (respectively, D. Sengupta et al. 2024, N. Torres-Albà et al. 2025, in preparation), due to the large number of observations available. This leaves us with 13 sources that are studied in this work. A list of the total 52 observations analyzed in this paper is presented in Table 1.

3. Data Reduction and X-Ray Spectral Analysis

The Chandra data were reduced with the CIAO (v4.14; A. Fruscione et al. 2006) software and the Chandra Calibration Data Base `caldb` 4.9.7 adopting standard procedures. The source and the background spectra were extracted using the CIAO `specextract` tool. For the source, we selected a circle of 5″; the background was extracted either from an annulus centered in the source or a circle positioned a few arcseconds away after a visual inspection to avoid the presence of any other source in the field. The spectra were grouped between 3 and 15 counts per bin (see Appendix D for details), using the `grppha` tool.

The XMM-Newton observations were reduced using the Science Analysis System (SAS; F. Jansen et al. 2001) version 20.0.0. For each observation, we inspected the light curve at energies $E > 10\,{\rm keV}$ in order to remove high particle background. We extracted the spectra from a region of 30″ for the source and 40″ for the background for all the detectors after visually inspecting each image to avoid contamination from nearby X-ray sources. Finally, we binned the spectra to have at least 15 counts per bin.

The Suzaku data were extracted following the ABC guide[12] from HEASARC. For each observation, we extracted the spectra from both the frontside (XI0, XI3) and backside (XI1) illuminated chips unit of the X-ray imaging spectrometers

[12] https://heasarc.gsfc.nasa.gov/docs/suzaku/analysis/abc/

Table 1
Observation Details and Properties of the Sources Analyzed in This Work

Source Name	R.A. J2000	Decl. J2000	Redshift	Instrument	ObsID	Exposure Time (ks)	Obs Date
(1)	(2)	(3)	(4)	(5)	(6)	(7)	(8)
NGC 454E	01:14:24.93	−55:23:49.31	0.012	Suzaku	704009010	128.95	2009-04-29
				XMM-Newton	0605090301	29.9	2009-11-05
				Chandra - 1	13891	5.1	2012-02-19
				NuSTAR - 1	60061009002	24.2	2016-02-14
				NuSTAR - 2	60760003002	25.4	2021-02-14
				Chandra - 2	23812	15.1	2021-02-14
MRK 348	00:48:47.14	+31:57:25.08	0.015	XMM-Newton - 1	0067540201	49.5	2002-07-18
				Suzaku	703029010	87.5	2008-06-28
				Chandra	12809	95.0	2010-10-13
				XMM-Newton - 2	0701180101	13.1	2013-01-04
				NuSTAR - 1	60160026002	21.5	2015-10-28
				NuSTAR - 2	60701017002	104.8	2022-02-06
NGC 4992	13:09:05.59	+11:38:02.82	0.025	Chandra - 1	6277	3.7	2005-07-25
				Suzaku	701080010	38.8	2006-06-18
				XMM-Newton	0312192101	16.4	2006-06-27
				NuSTAR - 1	60061239002	23.5	2015-01-27
				Chandra - 2	23707	6.3	2021-04-04
ESO 383-18	13:33:26.10	-34:00:53.31	0.012	XMM-Newton	0307000901	16.1	2006-01-10
				NuSTAR - 1	60061243002	17.3	2014-09-11
				NuSTAR - 2	60261002002	106.5	2016-01-20
				Chandra	23687	2.1	2021-04-03
MRK 417	10:49:30.92	+22:57:52.37	0.032	XMM-Newton	0312191501	14.3	2006-06-15
				Suzaku	702078010	41.5	2007-05-18
				NuSTAR	60061206002	20.7	2017-02-20
				Chandra	23724	5.7	2022-07-10
MCG-01-05-047	01:52:49.004	-0.3:26:48.56	0.017	Suzaku	704043010	46.9	2009-06-25
				XMM-Newton	0602560101	14.9	2009-07-24
				NuSTAR	60061016002	13.4	2012-11-30
				Chandra	26146	10.1	2021-10-10
ESO 103-35	18:38:20.32	-65:25:39.14	0.013	XMM-Newton	0109130601	12.9	2002-03-15
				Suzaku	703031010	91.4	2008-10-22
				NuSTAR - 1	60061288002	27.3	2013-02-24
				NuSTAR - 2	60301004002	43.8	2017-10-15
NGC 1142	02:55:12.23	-00:11:00.80	0.028	XMM-Newton	0312190401	11.9	2006-01-28
				Suzaku - 2	701013010	101.6	2007-01-23
				Suzaku - 1	702079010	40.6	2007-07-21
				NuSTAR	60368001002	20.7	2017-10-14
IRAS 16288+3929	16:30:32.65	39:23:3.15	0.030	Suzaku	806150010	18.7	2011-08-18
				XMM-Newton	0671900101	31.0	2011-09-08
				NuSTAR	60061271002	16.1	2012-09-19
ESO 263-13	10:09:48.21	-42:48:40.4	0.032	Suzaku	702120010	45.3	2007-06-01
				XMM-Newton	0501210101	26.3	2007-06-14
				NuSTAR	60061098002	22.8	2015-10-13
Fairall 272	08:23:01.10	-4:56:5.50	0.022	XMM-Newton	0501210501	11.914	2007-10-14
				NuSTAR	60061080002	24.3	2014-01-10
				Chandra	23703	2.9	2021-03-28
LEDA 2816387	3:56:19.97	-62:51:28.73	0.107	NuSTAR - 1	60201034002	26.5	2016-05-06
				XMM-Newton	0802450201	21.0	2017-11-20
				NuSTAR - 2	60160172002	24.6	2021-06-04
2MASX J06411806+3249313	6:41:18.04	+32:49:31.6	0.047	XMM-Newton	0312190901	13.9	2006-03-11
				Chandra	22040	10.1	2018-12-25
				NuSTAR	60061071002	18.3	2018-12-31

Note. (1) Source name; (2) and (3) source R.A. and Dec (J2000 Epoch); (4) source redshift from NED (NASA/IPAC extragalactic database https://ned.ipac.caltech.edu/); (5) telescope used in the analysis; (6) observation ID; (7) nominal exposure time in ks; (8) observation starting date. The sources are arranged in descending order based on the number of observations.

(XIS) running the aepipeline. To extract the spectra, we used a region of 60″–260″ depending on the source.[13] The response, ancillary and background files were generated running the tasks xisrmfgen, xissimarfgen, and xisnxbgen, respectively. We then grouped the data to a minimum of 25 counts per bin.

The NuSTAR data were retrieved from both focal plane modules, FPMA and FPMB. The event data files were calibrated and cleaned using the NuSTAR nupipeline script version 0.4.8. and the Calibration Database (CALDB) v.20210427 as response file. Then, we used the nuproducts script to generate the ARF, RMF and light-curve files. The source spectrum was extracted from a 75″ circular region centered on the source's optical position. After a visual inspection, we used a region of the same size to extract the background spectrum from each module to avoid contamination from other sources. Finally, the NuSTAR spectra were grouped with the grppha task with a minimum of 15 counts per bin.

3.1. X-Ray Spectral Analysis

The X-ray spectra were analyzed in XSPEC K. A. Arnaud (1996) version 12.12.1 in HEASOFT version 6.30.1.

We analyzed the torus properties of each source in the sample by simultaneously fitting the X-ray spectra using three models based on Monte Carlo simulations that can self-consistently describe the primary AGN emission with the CT gas ($N_{\rm H,los} > 1.5 \times 10^{24}\,{\rm cm}^{-2}$) in the surrounding torus. The three torus models used in this work are borus02 (M. Baloković et al. 2018), MYTorus (K. D. Murphy & T. Yaqoob 2009; T. Yaqoob 2012), and UXCLUMPY (J. Buchner et al. 2019).

To all models, we add a collisionally ionized diffuse gas emission component (apec, R. K. Smith et al. 2001) in order to account for the soft (<2 keV) X-ray emission from the central region of the host galaxy. The galactic absorptions measured by P. M. W. Kalberla et al. (2005) are included to consider the absorption due to the gas in the Milky Way ($\sim 10^{20}\,{\rm cm}^{-2}$). Finally, we model the fraction of the intrinsic AGN power law that is scattered without being reprocessed by the obscuring material by multiplying the intrinsic power law (cutoffpl in the model) by the fraction of the scattered emission, F_s. To account for intrinsic flux variability between different epochs, we apply a multiplicative factor, $C_{\rm AGN}$, to the intrinsic power-law model.

In XSPEC notation, the source model is defined as:

$$\begin{aligned}\text{Model} = \text{phabs} * \{\text{apec} + C_{\rm AGN} * (\text{TorusModel} + \\ + F_{\rm s} * \text{cutoffpl})\}. \end{aligned} \quad (1)$$

Here, the TorusModel is one of the aforementioned torus models.

All the models are fitted in the 0.6[14]–30/70 keV range, depending on the energy at which the NuSTAR background counts overtook the source emission for each source. To be consistent with M. Baloković et al. (2020) and their study on the high-energy cutoff of local obscured AGN, we froze the high-energy cutoff for all three models to 300 keV. Furthermore, using only NuSTAR data (up to 70 keV in a best-case scenario), we would be unable to constrain the cutoff energy.

[13] Following the recommendation on the region selection in the ABC guide.
[14] The MYTorus model is not accurate below 0.6 keV.

3.2. Borus02

The borus02 model assumes a uniform-density sphere with two conical cutouts filled with a cold, neutral, static medium with solar abundance. In this model, the line-of-sight inclination angle θ_i and the covering factor C_F (the fraction of the sky covered by the torus as seen from the central engine) are variable parameters.

Since borus02 models only the reflection component of the AGN emission, which accounts for the Compton hump and the fluorescent emission lines, the absorption of the torus clouds and the scattered component were added manually.

In XSPEC, the model has the following configuration:

$$\begin{aligned}\text{TorusModel} = \text{borus02\_v170323a.fits} + \\ + \text{zphabs} * \text{cabs} * \text{cutoffpl}. \end{aligned} \quad (2)$$

where zpbabs and cabs account for the photoelectric absorption due to the cold medium and the Compton-scattering losses along the line of sight, respectively.

3.3. MYTorus

The MYTorus model considers a cylindrical, azimuthally symmetric torus with a fixed half-opening angle of 60°, filled with a uniform neutral cold reprocessing material. In this model, the main components of an obscured AGN X-ray spectrum (the line of sight, the reflection, and the fluorescent emission line component) are treated self-consistently by the use of three different tables, as can be seen in Equation (3). The Compton-scattered and the emission lines components are weighted differently by adding multiplicative constants A_S and A_L, respectively.

In this work, we use the model in the decoupled configuration (T. Yaqoob 2012; T. Yaqoob et al. 2015), which allows the disentanglement of the line-of-sight column density from the average one ($N_{\rm H,av}$). In the decoupled configuration, the zeroth-order continuum (the continuum photons that escaped the torus without being scattered) is independent of the inclination angle, which is fixed to be $\theta_i = 90°$. In this way, the zeroth-order continuum is independent of geometry and becomes a line-of-sight quantity. In order to take the possible patchiness and configurations of the torus and of the consequent Compton scattering and lines features into account, these two components are considered both in an edge-on and face-on configuration. In the first case, the inclination angle, set to be $\theta_{i,S,L} = 90°$, mimics the forward scattering and it is weighted by $A_{S,L90}$; this means that we are accounting for a more uniform torus because the photons are primarily reprocessed by the obscuring material that is lying between the AGN and the observer. In the second case, $\theta_{i,S,L} = 0°$ accounts for a backward scattering and $A_{S,L0}$ is the weighting constant. This second scenario is more likely to happen when the torus presents a more patchy structure, in which the photons scattered by the backside of the torus have less chance to interact again with the material before reaching the observer. When $A_{S,L90}$ and $A_{S,L0}$ are left free to vary, we refer to the configuration as "decoupled free," and a ratio between the two constants can give a qualitative idea of which emission is more prominent, thus giving us an indication of the inclination angle of the torus. In addition, a ratio between $N_{\rm H,los}/N_{\rm H,av}$ can approximate the clumpiness of the torus.

In XSPEC, the model is as follows:

$$\begin{aligned}\text{TorusModel} = &\ \text{mytorus\_Ezero\_v00.fits} * \text{zpowerlw} + \\ &+ A_{S,0} * \text{mytorus\_scatteredH300\_v00.fits} + \\ &+ A_{L,0} * \text{mytl\_V000010nEp000H300\_v00.fits} + \\ &+ A_{S,90} * \text{mytorus\_scatteredH300\_v00.fits} + \\ &+ A_{L,90} * \text{mytl\_V000010nEp000H300\_v00.fits}. \end{aligned} \quad (3)$$

3.4. UXCLUMPY

UXCLUMPY (J. Buchner et al. 2019) is a model that was constructed to reproduce and model the column density and the cloud eclipsing events in AGN tori in terms of their angular sizes and frequency.

UXCLUMPY mainly differs from the two aforementioned models in that the torus clumpiness and the cloud dispersion are included in the model. Indeed, the model is constructed to reproduce a cloud distribution with different hydrogen column densities based on observed eclipse event rates (A. G. Markowitz et al. 2014; J. Buchner et al. 2019) assuming the clouds to be on circular Keplerian orbits on random planes, for simplicity. The dispersion of the distribution is modulated by TORσ ($\sigma \in [0\text{–}84]$), where a large value stands for a large dispersion of the clouds. To model strong reflection features (see, e.g., A. Pizzetti et al. 2022), UXCLUMPY allows for an additional inner ring of CT material, whose covering factor is measured by the CTKcover parameter (CTKcover $\in [0\text{–}0.6]$). Both TORσ and CTKcover provide a powerful, consistent way to probe the torus geometry by modeling the clouds and the extension of the reflector. TORσ, CTKcover, and the line-of-sight inclination angle θ_i are free parameters during the fit.

In the previously discussed model geometries, $N_{\rm H,av}$ and $N_{\rm H,los}$ are closely related. In contrast, UXCLUMPY is a unified obscurer model, where one clumpy torus geometry defined by TORσ and CTKcover can be observed under a wide range of $N_{\rm H,los}$ (10^{20}–10^{26} cm^{-2}). The corresponding equatorial hydrogen column density $N_{\rm H,eq}$ has so far not yet been published. For comparison with the other models, we compute for each TORσ and CTKcover combination the $N_{\rm H,eq}$ in Section 5.1.

In XSPEC, the model is as follows:

$$\begin{aligned}\text{TorusModel} = &\ \text{uxclumpy-cutoff.fits} + \\ &+ F_s * \text{uxclumpy-cutoff-omni.fits}. \end{aligned} \quad (4)$$

The first table includes the torus transmitted and reflected component. In contrast, the second one, multiplied by the scattering fraction, takes into account the presence of a warm mirror emitter, a volume-filling gas between the clumps that is, in part, responsible for the scattering of the intrinsic AGN power law.

4. Variability Estimates

In this section, we briefly summarized the method we implemented to measure the $N_{\rm H,los}$ variability in the studied sample. For a complete explanation, we invite the reader to check Section 5 of NTA23. The method proposed by NTA23 and reported below uses two different estimators of source variability, the reduced χ^2 ($\chi^2_{\rm red}$) and the p-value.

4.1. Reduced χ^2/reduced Stat Comparison

To test for variability, we compare the $\chi^2_{\rm red}$ of the best fit to the X-ray data performed with xspec (which assumes both intrinsic flux and $N_{\rm H,los}$ variability) to the best possible fits performed when fitting the data under three assumptions: (1) no variability at any epoch is taken into account, either in intrinsic flux or $N_{\rm H,los}$, ($\chi^2_{\rm red}$ No Var); 2) only $N_{\rm H,los}$ variability is considered ($\chi^2_{\rm red}$ No $C_{\rm AGN}$ Var); (3) only intrinsic flux variability at any epoch is considered ($\chi^2_{\rm red}$ No $N_{\rm H,los}$ Var). We then define a tension between the data and the model as $T = |1 - \chi^2_{\rm red}|/\sigma$, where $\sigma = 1/\sqrt{N}$ is the standard deviation of the Gaussian that best represents the χ^2 distribution, and N is the number of degrees of freedom of the spectral fit. We consider model A to fit a source significantly better than model B when $T_{\rm A} < 3$ and $T_{\rm B} > 5$ (see R. Andrae et al. 2010, for more details).

This method classifies sources as $N_{\rm H,los}$-variable by comparing the best-fit T with the non-$N_{\rm H,los}$-variable T. If both models yield a $T < 3$, we classify the source as nonvariable in $N_{\rm H,los}$ because $N_{\rm H,los}$ variability is not required to fit the data. Similarly, in the case where both models (variable and nonvariable) return $T > 5$, we consider the difference in the significance between the two models and discuss whether the inclusion of $N_{\rm H,los}$-variability improves the fit or not (see, e.g., NGC 4388 in NTA23, ESO 383-18 and ESO 263-18 in D.4, D.10, respectively). We classify the source as "Undetermined" when the three torus models yield different classifications. We note that in the cases in which the reduced statistics is used, the distribution does not necessarily follow a Gaussian, as the χ^2 does for a large number of degrees of freedom. Thus, the interpretation of T in such cases is not straightforward. We still provide the value as a reference.

We note that, for some sources, a combination of χ^2 and C-statistics was applied to fit the data (see individual source comments in Appendix D). In such cases, we use reduced stat instead of $\chi^2_{\rm red}$. The reduced χ^2/reduced stat and p-values for each source and all models are listed in Table 2 and Tables 5 through 16.

4.2. p-value

We estimate the probability that the source is nonvariable in $N_{\rm H,los}$ (null hypothesis) by computing a new χ^2, defined as follows:

$$\chi^2_{N_H} = \sum_i \frac{(\rm N_{H,los,i} - \langle N_{H,los}\rangle)^2}{\delta(\rm N_{H,los,i})^2}. \quad (5)$$

which derives from fitting the $N_{\rm H,los}$ for all epochs, for each source ($N_{\rm H,los,i}$) to the average $N_{\rm H,los}$ for that source ($\langle N_{\rm H,los}\rangle$). The χ^2 is then converted into a p-value (null hypothesis: the source is not $N_{\rm H,los}$-Variable) by following the method described in NTA23. We classify the source as "$N_{\rm H,los}$ variable" if p-value < 0.01 for all the three models used, and as "nonvariable in $N_{\rm H,los}$" if p-value > 0.01. We classify the source as "undetermined" if the three models are in disagreement, i.e., the p-value is above the threshold for one model and below for the others.

The final source classification is reported in Table 4, in which we compare the $\chi^2_{\rm red}$ and the p-value results for each model. We classify the source as "undetermined" when the two

Table 2
X-Ray Fitting Results for 2MASX J06411806+3249313

Parameter		borus02	MYTorus dec	UXCLUMPY
stat/d.o.f[a]		500.44/542	499.72/543	509.73/541
red stat[b]		0.92	0.92	0.94
T[c]		1.78	1.85	1.34
p-value[d]		0.60	0.55	0.37
kT[e]		…	…	…
apec norm($\times 10^{-4}$)[f]		…	…	…
Γ[g]		$1.55^{+0.09}_{-0.07}$	$1.73^{+0.12}_{-0.13}$	$1.77^{+0.05}_{-0.06}$
$N_{\rm H,av} \times 10^{24}$ cm$^{-2(h)}$		$0.09^{+0.19}_{-0.05}$	$0.35^{+0.16}_{-0.16}$	…
C_F[i]		$0.79^{+0.14}_{-0.45}$	…	…
$\cos(\theta_i)$[j]		0.95^{+u}_{-u}	…	…
θ_i[k]		…	…	<11.01
CTKcover[l]		…	…	$0.36^{+0.02}_{-0.03}$
TORσ[m]		…	…	<2.36
$A_{S,90}$[n]		…	$0.08^{+0.41}_{-0.06}$	…
$A_{S,0}$[o]		…	$11.63^{+10.57}_{-5.86}$	…
F_s($\times 10^{-3}$)[p]		$6.47^{+2.79}_{-2.79}$	$6.45^{+4.07}_{-4.03}$	$6.72^{+7.59}_{-1.47}$
Norm (10^{-3})[q]		$1.85^{+0.48}_{-0.33}$	$1.61^{+0.37}_{-0.29}$	$6.05^{+1.86}_{-1.13}$
$C_{\rm AGN}$[r]	XMM-Newton	$0.68^{+0.08}_{-0.07}$	$0.67^{+0.07}_{-0.06}$	$0.76^{+0.23}_{-0.11}$
	Chandra	$0.99^{+0.14}_{-0.12}$	$1.00^{+0.12}_{-0.11}$	$1.13^{+0.34}_{-0.18}$
	NuSTAR	1	1	1
$N_{\rm H,los} \times 10^{22}$[s]	XMM-Newton	$15.53^{+1.90}_{-1.73}$	$14.69^{+4.27}_{-2.09}$	$14.02^{+1.77}_{-0.72}$
	Chandra	$14.29^{+1.93}_{-1.74}$	$13.35^{+3.94}_{-2.03}$	$13.65^{+1.59}_{-0.98}$
	NuSTAR	$11.51^{+2.36}_{-2.10}$	$9.03^{+3.44}_{-2.49}$	$11.68^{+0.94}_{-1.41}$
log $L^{t}_{\rm NuSTAR,2-10\ keV}$		$43.68^{+0.05}_{-0.05}$	$43.47^{+0.08}_{-0.08}$	44.08
log $L^{u}_{\rm NuSTAR,10-40\ keV}$		$43.56^{+0.04}_{-0.04}$	$43.04^{+0.03}_{-0.23}$	44.11
Red stat - No Var.[v]		1.50	1.49	1.57
T		11.72	11.67	13.54
Red stat - No $C_{\rm AGN}$Var.[w]		0.98	0.96	0.95
T		0.47	0.87	1.07
Red stat - No $N_{\rm H,los}$ Var.[x]		0.93	0.93	0.96
T		1.57	1.54	0.91

Notes.
[a] Statistic (or χ^2) over degree of freedom. We refer to "Stat" as a combination of C-stat and χ^2 statistics.
[b] Reduced statistic (or χ^2).
[c] Statistical tension between the data and the model.
[d] p-value where the null hypothesis is that no $N_{\rm H,los}$ variability is found among different observations of the source.
[e] apec model temperature in units of keV.
[f] apec model normalization.
[g] Power law photon index.
[h] Torus's average hydrogen column density in units of 10^{24} cm^{-2}.
[i] Covering factor of the torus, as fitted by borus02.
[j] Cosine of the inclination angle, as fitted by borus02. $\cos(\theta_i) = 0$ represents an edge-on scenario.
[k] Inclination angle, as fitted by UXCLUMPY. $(\theta_i) = 90$ represents an edge-on scenario.
[l] Covering factor of the inner ring of clouds, as fitted by UXCLUMPY.
[m] Cloud dispersion factor, as fitted by UXCLUMPY.
[n] Reflection component constant associated with an edge-on scenario, as fitted by MYTorus.
[o] Reflection component constant associated with a face-on scenario, as fitted by MYTorus.
[p] Scattering fraction.
[q] Normalization of the intrinsic AGN power law.
[r] Cross normalization factor between observations with respect to the first NuSTAR observation, for which $C_{\rm AGN}$ is fixed to 1.
[s] Line-of-sight hydrogen column density of the torus in units of 10^{22} cm^{-2}.
[t] Logarithm of the intrinsic luminosity of the first NuSTAR observation in the 2–10 keV regime.
[u] Logarithm of the intrinsic luminosity of the first NuSTAR observation in the 10–40 keV regime.
[v] Reduced statistic (or χ^2) and tension when no variability is considered.
[w] Reduced statistic (or χ^2) and tension when no flux variability is considered.
[x] Reduced statistic (or χ^2) and tension when no $N_{\rm H,los}$ variability is considered. We use a dash when the whole spectral component is missing and three dots when the parameter is not computed by the model. A whole column is missing when that model is not used to fit the source.

methods or the different fitting models disagree in the classification.

5. Results and Discussion

In this section, we present the result of the X-ray spectral analysis performed on the 13 galaxies of the sample. We perform a simultaneous multiepoch fit for each galaxy using the three models described above. We display the best-fit results (Table 2), the `borus02` best-fit spectrum (Figure 1) and the $N_{H,los}$-variability plot (Figure 2) for 2MASX J06411806 +3249313 (2MASX J06411806 hereafter). The best-fit values, the `borus02` best-fit spectra and $N_{H,los}$-variability plots for the remaining 12 sources are reported in Appendix A, B and C, respectively. The comments on each individual source are reported in Appendix D.

The best-fit values for each model for 2MASX J0641180 are reported in Table 2 and are tabulated as follows: the first section reports the best-fit statistics (stat/degree of freedom and reduced statistics), as well as the *p*-value and tension T between the data and the best fit, derived as described in Section 4. The second block reports the best-fit soft-emission properties. In the third section, we report the best-fit torus parameters, such as the covering factor, the inclination angle, and the cloud dispersion. The fourth and fifth sections report the variability measurements in intrinsic flux (C_{AGN}) and $N_{H,los}$ measured in the fitting process. The sixth section reports the logarithm of the intrinsic luminosity for the first NuSTAR observation in two energy ranges, 2–10 keV and 10–40 keV. The luminosity at any other epoch can be obtained by multiplying this value by the cross-normalization factor. The last three panels report the statistical analysis (reduced statistics and tension) derived by considering: (1) no variability (either intrinsic flux or $N_{H,los}$) at any epochs; (2) no intrinsic flux variability between the observations (i.e., the fit is performed by allowing only $N_{H,los}$ variability); and (3) no line-of-sight hydrogen column density variability is allowed between the observations (i.e., only intrinsic flux variability is permitted). By comparing the best-fit tension to the nonvariable one, we can affirm that all of the sources require variability, either in intrinsic flux or $N_{H,los}$.

5.1. Equatorial Hydrogen Column Density - UXCLUMPY

This section presents the computation of the equatorial column densities for `UXCLUMPY`. The `UXCLUMPY` X-ray spectral model library consists of two parameters that define the clumpy torus geometry: TORσ and CTKcover. A grid of possible geometries was created by J. Buchner et al. (2019), by generating a population of spherical blobs. J. Buchner et al. (2019) presented the angle-averaged column density distribution. This is achieved by sampling many directions from the center (the location of the X-ray corona) and computing the column density. Based on the same information, P. G. Boorman et al. (2024) presented the covering factor for various column densities. Here, we analyze the column density distribution in the equatorial plane, averaged over azimuthal angles. This is achieved with the same sampling approach, but only within the equatorial plane.

The results are presented in Table 3. When the covering factor of the inner ring of CT clouds (CTKcover) is above 0.2, the equatorial column densities are CT. At lower values, e.g., CTKcover=0, the equatorial plane is dominated by the cloud population. At TORσ=0, there is no obscurer at all; therefore, the column density is equal to 10^{20} cm^{-2}, which is the typical obscuration given by the host galaxy. At TOR$\sigma > 0$, the column density increases with decreasing TORσ because more clouds lie along the equatorial sightlines. In contrast, in the uniform density models `borus02` and `MYTorus`, the $N_{H,av}$ is not related to the opening angle in the same way, and rather sets the column density of the entire Compton reflecting material directly. This may explain the differences in the inferred $N_{H,eq}$ and $N_{H,av}$. The code to compute $N_{H,eq}$ starting from best-fit values of TORσ and CTKcover can be found at Zenodo, DOI:10.5281/zenodo.14247269.

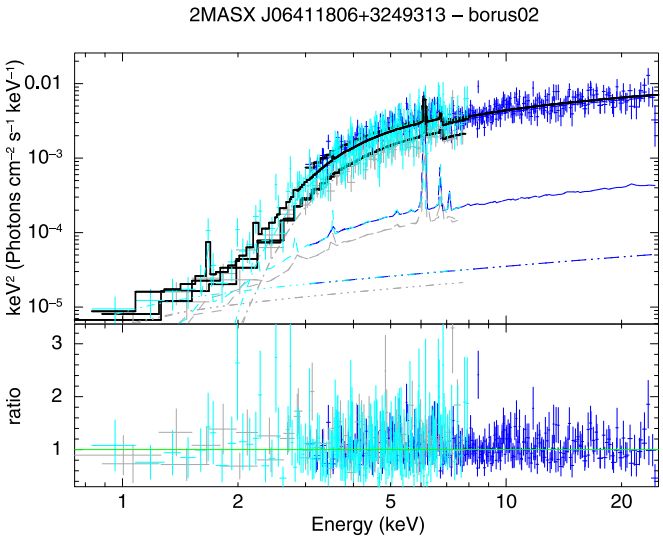

Figure 1. Unfolded Chandra (cyan), XMM-Newton (gray), and NuSTAR (blue) 0.6–25 keV combined spectrum of 2MASX J06411806 modeled with `borus02`. The best-fit model is plotted with a solid black line. Reflection: Dashed. Line-of-sight: Dashed–dotted. Scattering: Dashed–dotted-dot-dot.

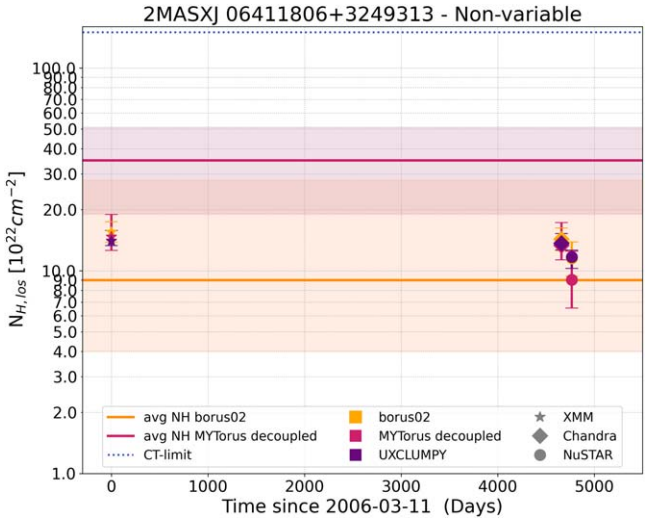

Figure 2. $N_{H,los}$ ($\times 10^{22}$ cm^{-2}) of 2MASX J06411806 as function of time for `borus02`, `MYTorus` and `UXCLUMPY`. Solid lines and shaded areas represent $N_{H,av}$ and associated uncertainties for `MYTorus` and `borus02`. The blue dotted line corresponds to the CT limit (150 $\times$ 10^{22} cm^{-2}).

5.2. Discussion

In this section, we discuss the results obtained from the variability analysis performed on the full sample of 27 galaxies,

Table 3
UXCLUMPY Equatorial Hydrogen Column Density ($N_{H,eq}$) Values for all the Sources Analyzed in This Study, in NTA23, in A. Pizzetti et al. (2022), and in D. Sengupta et al. (2024)

Source	TORσ (°)	CTKcover	$N_{H,eq}$ ($\times 10^{24}$ cm^{-2})
MRK 348	27.99	0	3.46
NGC 4992	28.18	0.30	41.67
ESO 383-18	7.90	0	11.65
MRK 417	9.39	0	10.65
MCG-01-05-047	27.23	0.21	40.36
ESO 103-35	81.83	0.34	39.95
NGC 1142	25.71	0.26	42.07
IRAS 16288-3929	70.00	0.57	37.58
ESO 263-13	7.03	0.25	52.46
Fairall 272	21.27	0.16	28.27
LEDA 2816387	7.03	0.27	52.94
2MASXJ 06411806	2.36	0.36	47.15
NGC 612	0.36	0.37	43.75
NGC 788	12.6	0	8.77
NGC 833	3.8	0	0.06
NGC 835	6.8	0	8.80
3C 105	15.9	0	7.19
4C+29	17.5	0	6.53
NGC 3281	28.0	0	3.46
NGC 4388	66.7	0	1.01
IC 4518A	84.0	0.29	38.54
3C 445	84.0	0	0.58
NGC 7319	77.9	0	0.71
3C 452	84.0	0	0.58
NGC 7479	24.6	0.6	43.43
NGC 6300	24.1	0.6	43.69

13 of which are analyzed in this paper, 12 in NTA23, one in A. Pizzetti et al. (2022) and one in D. Sengupta et al. (2024). All the sources were selected from a pool of potentially $N_{H,los}$ variable sources identified by XZ21; our sample is thus intentionally biased toward variable sources (either in $N_{H,los}$ or intrinsic flux).

Applying the method proposed by NTA23 and explained in Section 4, we are able to classify the sources as shown in Table 4 and Table 3 of NTA23. Although the sample is biased toward variable sources, as mentioned above, only 37% of the sources (10 out of 27) require $N_{H,los}$ variability between the observations, while for 44% of them (12 out of 27) we can confidently say that no $N_{H,los}$ variability is needed to reach a proper fit in the timeframe analyzed. For five sources, either intrinsic flux or $N_{H,los}$ variability is required, but the data are insufficient to confidently distinguish between the two scenarios; these sources are thus classified as "Undetermined." As proposed by NTA23, joint soft-hard X-ray observations could disentangle the two scenarios.

5.2.1. Line-of-sight Hydrogen Column Density Variability Over Time

Figure 2 shows the line-of-sight hydrogen column density as a function of time for 2MASX J06411806, classified as "Nonvariable in $N_{H,los}$." 2MASX J06411806 is the only galaxy of the sample for which we observe the $N_{H,los}$ values to lie within the range of average hydrogen column density, resembling the scenario observed by NTA23 for NGC 612, NGC 833, and 3C 105. The other sources, whose $N_{H,los}$ variability plots can be seen in Appendix C (Figures 8, 9), present two main behaviors: for 5 out of 13, the clouds ($N_{H,los}$) are denser than the average density of the torus, while for 6 out of 13 we observe the torus to be denser than the clouds; a similar denser torus has also been observed in NGC 7479 (A. Pizzetti et al. 2022). Similar to NGC 3281 in NTA23, MRK 417 exhibits characteristics aligning with both scenarios, depending on the considered model (see Section D.5 for more details).

The first scenario can be interpreted by considering the medium responsible for X-ray obscuration (the obscurer) as consisting of overdense clouds dispersed within a less dense intercloud medium, acting as a thin reflector. This scenario was previously suggested by NTA23, and it hypotheses that while the denser clouds also reflect, their reflection component (or thick reflector) is missed by the modeling due to its spectral shape being more similar to that of the line-of-sight component (see, Figure 3 in NTA23, for more details). This idea is consistent with the two-phase medium invoked by M. Stalevski et al. (2011) and R. Siebenmorgen et al. (2015) to explain infrared observations.

The second scenario, where the overall density of the torus exceeds the column density along the line of sight, can be explained by considering the reflector as an area of higher density positioned near the X-ray emitting region, while the obscurer represents an underdense cloud distribution. The absence of observed absorption by the reflector (otherwise resulting in solely higher line-of-sight column densities) can be explained if we consider it to be geometrically thin (i.e., a warped disk; see A. Lawrence & M. Elvis 2010, and Section 5.2.3 for more details), capable of intercepting a sufficient amount of incoming X-ray radiation to produce pronounced reflection features, yet permitting a portion of the radiation to be absorbed by the clouds (see, e.g., NGC 7479 in A. Pizzetti et al. 2022). Both cases favor a scenario where the media mainly responsible for absorption and reflection may be dissociated within the torus, as proposed in A. Pizzetti et al. (2022) and N. Torres-Albà et al. (2023). Interestingly, we do not find any correlation between the two scenarios and the variability class, between $N_{H,av}$ and the intrinsic luminosity (Pearson coefficient $= -0.21$), or between $N_{H,av}$ and the Eddington ratio (Pearson coefficient $= -0.18$).

5.2.2. Torus Properties as a Function of Variability Class

Figures 3 and 4 show bar plots of the averaged best-fit properties for all sources, grouped by variability class. Panel (a) displays the time-averaged value of the line-of-sight column density ($\langle N_{H,los} \rangle$), while panel (b) shows the average hydrogen column density of the torus; the difference between the two can be interpreted as an indicator of the torus clumpiness/inhomogeneity, i.e., the smaller the value, the more homogeneous the torus, see panel (c). The geometrical properties of the torus, such as the inclination angle, the covering factor, and the cloud dispersion of the torus, are shown in panels (d), (e), and (f), respectively. Intrinsic AGN properties, such as the 2–10 keV luminosity and the Eddington ratio are shown in panels (g) and (h). To obtain the Eddington ratio $\lambda_{Edd} = L_{Bol}/L_{Edd}$, we first computed the bolometric luminosity for each source by applying the bolometric correction reported in R. V. Vasudevan et al. (2010) to $L_{2-10\,keV}$. We then divided this value with the Eddington luminosity $L_{Edd} = \frac{4\pi G M_{BH} m_p c}{\sigma_T}$, where m_p is the mass of the proton, M_{BH} is the mass of the black hole as reported in M. J. Koss et al. (2022), and σ_T is the Thompson cross section. As seen in the bar plot, there does not

Table 4
$N_{H,los}$ Variability Results

Source	borus02		MYTorus		UXCLUMPY		Classification
	χ^2_{red}	p-val.	χ^2_{red}	p-val.	χ^2_{red}	p-val.	
NGC 454E	Y*	Y	Y	Y	…	…	Variable
MRK 348	Y*	Y	Y*	Y	Y*	Y	Variable
NGC 4992	N	N	N	N	N	N	Nonvariable
ESO 383-18	N	N	N	N	N	N	Nonvariable
MRK 417	N	N	N	N	N	N	Nonvariable
MCG-01-05-047	N	N	Y	Y	N	N	Undetermined
ESO 103-35	Y	N	N	N	Y	N	Undetermined
NGC 1142	Y	Y	Y	Y	Y	Y	Variable
IRAS 16288+3929	Y	Y	Y	Y	Y	Y	Variable
ESO 263-13	Y*	Y	Y*	Y	Y*	Y	Variable
Fairall 272	Y	Y	Y	Y	N	N	Undetermined
LEDA 2816387	N	N	N	N	N	N	Nonvariable
2MASX J06411806+3249313	N	N	N	N	N	N	Nonvariable
NGC 7479	N	N	N	N	N	N	Nonvariable
NGC 6300	N	N	N	N	N	N	Nonvariable

Note. $N_{H,los}$-variability determinations using the χ^2_{red} and the p-value methods described in Section 4. N: Nonvariable. Y: Variable. Y*: Variable, see Appendix D for details. See A. Pizzetti et al. (2022) and D. Sengupta et al. (2024) for details about NGC 7479 and NGC 6300, respectively. No reliable fit was obtained for NGC 454E using UXCLUMPY (see D.1 for more details.)

seem to be any substantial difference between the three classes of variability.

Upon initial inspection of the plots, it becomes evident that, within errors, there appears to be no discernible distinction among the three populations. Applying the Anderson–Darling test[15] (M. A. Stephens 1974) to the three data sets for each best-fit property, the three samples are compatible with originating from the same parent population, requiring no intrinsic difference between the sources classified as variable, nonvariable, or undetermined. This is in contrast to the tentative trends suggested by NTA23 when analyzing the first 12 sources, which suggested there may be a trend for variable sources to have higher average obscuration and broader cloud distributions.

This lack of difference between the variability classes may point to two different scenarios. One scenario could involve distinguishing between sources with variable hydrogen column density ($N_{H,los}$ variable) and those without (nonvariable in $N_{H,los}$), yet their average geometric characteristics show no significant distinctions. This leads us to inquire about the underlying causes of the observed variability or its absence. Another possibility would be that the absence of detected variability in $N_{H,los}$ does not necessarily imply that the $N_{H,los}$ of the source has remained constant over time. Instead, it indicates that within the timeframe and the spectral quality examined in this study, variations in $N_{H,los}$ were not observed. However, it remains uncertain whether it is likely to detect sources exhibiting no variability across multiple observations spanning several years (see, e.g., NGC 7479 in A. Pizzetti et al. 2022 or 3C 445 in NTA23), while others demonstrate variability between each observation, occurring at various possible timescales (see, e.g., NGC 4388 in NTA23). Future targeted monitoring campaigns and a larger sample will help discern between the two proposed scenarios.

5.2.3. Inner Reflector and Water Megamaser Disks

As proposed in J. Buchner et al. (2019), and shown in A. Pizzetti et al. (2022) and N. Torres-Albà et al. (2023), a sole clumpy model is an inadequate description of the broad X-ray spectra of certain nearby obscured AGN. Indeed, an additional component consisting of dense ($N_{H,los} > 10^{25}\,cm^{-2}$) reflecting material is required to reproduce the Compton hump (peaking around ~20–50 keV) observed in some local obscured AGN. This dense inner ring is predicted to be on the inner side of the torus-accretion disk transition, although neither observational nor spectral data have yet confirmed its presence, position, or size (see A. Pizzetti et al. 2025, in preparation for insights into an ALMA campaign aimed at locating the putative inner ring in NGC 7479). Among the sources discussed in this work, 13 out of 27 (~48%) require the inclusion of the aforementioned inner ring in the fitting process. Notably, only one (NGC 7479) is CT, with the remaining 26 sources being Compton-thin. This scenario, featuring a CT reflector and Compton-thin absorber, could be explained by considering the distinction between the torus medium responsible for the reflection (inner ring) and the absorption (clouds) and assuming a warped geometry of the inner ring, as proposed by J. Buchner et al. (2019) and J. Buchner et al. (2021). Warped disk geometries naturally arise from nonplanar accretion (for a review see, J. A. Petterson 1977), and have been proposed to be the source of CT obscuration and reflection (i.e., A. Lawrence & M. Elvis 2010; J. Buchner et al. 2021). Notoriously, the 22 GHz water megamaser[16] disks are known to be warped (see, e.g., L. J. Greenhill et al. 2003b, 2023b; J. R. Herrnstein et al. 2005; C. Y. Kuo et al. 2011). The 22 GHz maser line emitted by water molecules originates in high-density regions in the innermost part of the nuclear structure. A. Masini et al. (2016) localized the maser disk to be outside the accretion disk, i.e., within the torus. This is supported by considering that the presence of water molecules requires a dense ($n_{H_2} \gtrsim 10^7\,cm^{-3}$, N. Bennert et al. 2004) dusty environment,

[15] The Anderson–Darling test probes whether two samples originate from the same parent population.

[16] Extragalactic water masers are generally called megamasers because of their high luminosity with respect to Galactic masers (A. Masini et al. 2016).

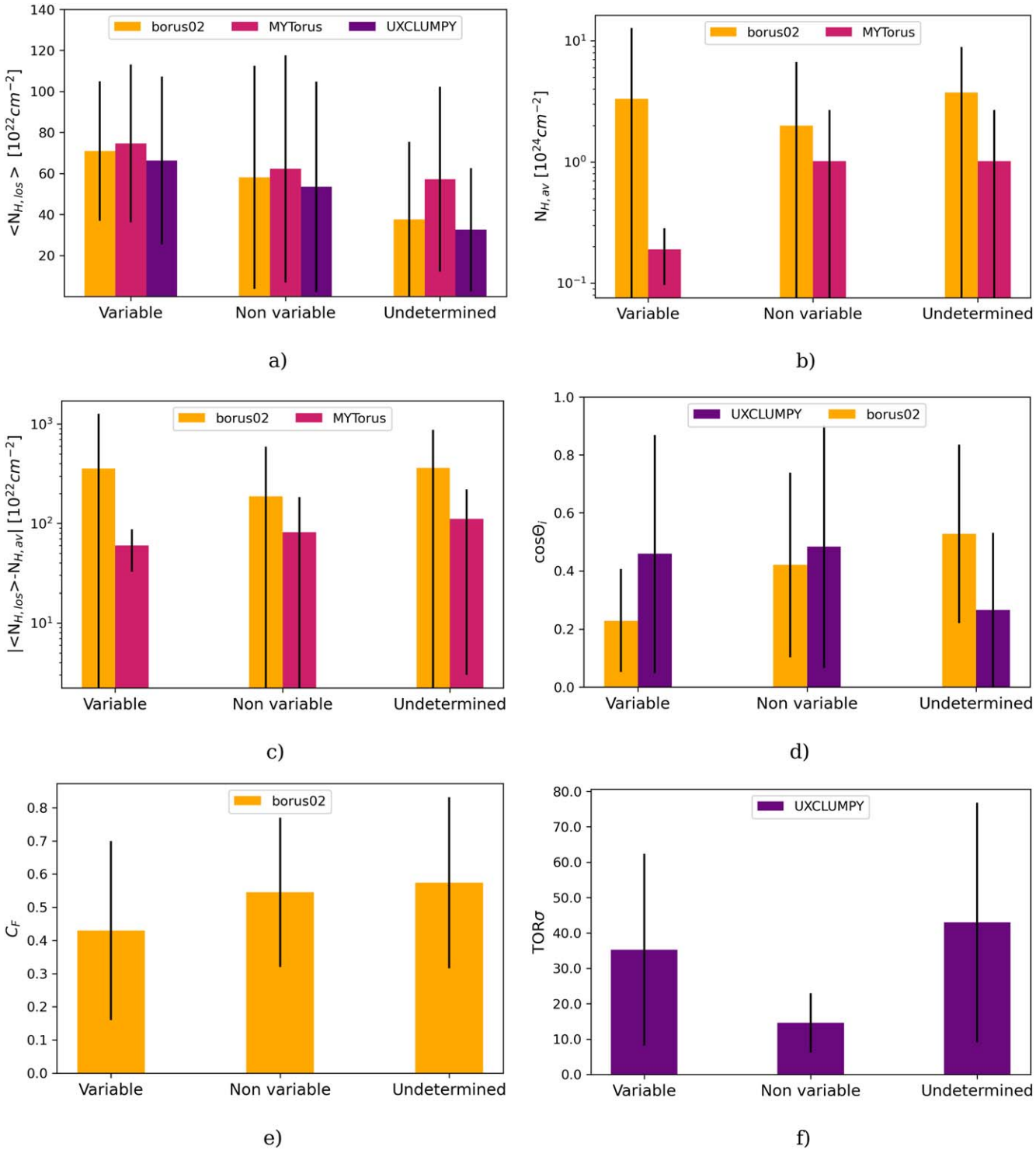

Figure 3. Bar plots displaying the averaged best-fit values for all sources, binned by variability class. The average of each parameter is computed across the sources within each variability class, with the error bar representing the standard deviation of each distribution. The models are color-coded as follows: yellow for `borus02`, magenta for `MYTorus`, and violet for `UXCLUMPY`. (a) Time average of the $N_{\rm H,los}$ for each single source. (b) Average hydrogen column density (to be considered as the column density of the reflector). (c) Absolute value of the difference between the average $N_{\rm H,los}$ and $N_{\rm H,av}$. (d) Cosine of the torus inclination angle as measured by `borus02` and `UXCLUMPY`. (e) Covering factor as computed by `borus02`. (f) Cloud dispersion (TORσ) as computed by `UXCLUMPY`.

positioning the maser disk outside the dust sublimation radius. Such findings imply a potential shared nature, or at least common geometrical and spatial properties, between the thick inner reflector and the water megamaser disks, as proposed by J. Buchner et al. (2021), particularly given that the majority of water megamasers are detected in Seyfert 2 and CT AGN (L. J. Greenhill et al. 2008).

Among the galaxies requiring the inner ring in their fit, approximately 30% (4[17] out of 13) exhibit recorded water megamaser emission—ESO 103-35 J. A. Braatz et al. (1996), NGC 6300 L. J. Greenhill et al. (2003b), NGC 7479

[17] We do not include MRK 348 because it hosts a "jet" megamaser, rather than a disk maser (A. B. Peck et al. 2003).

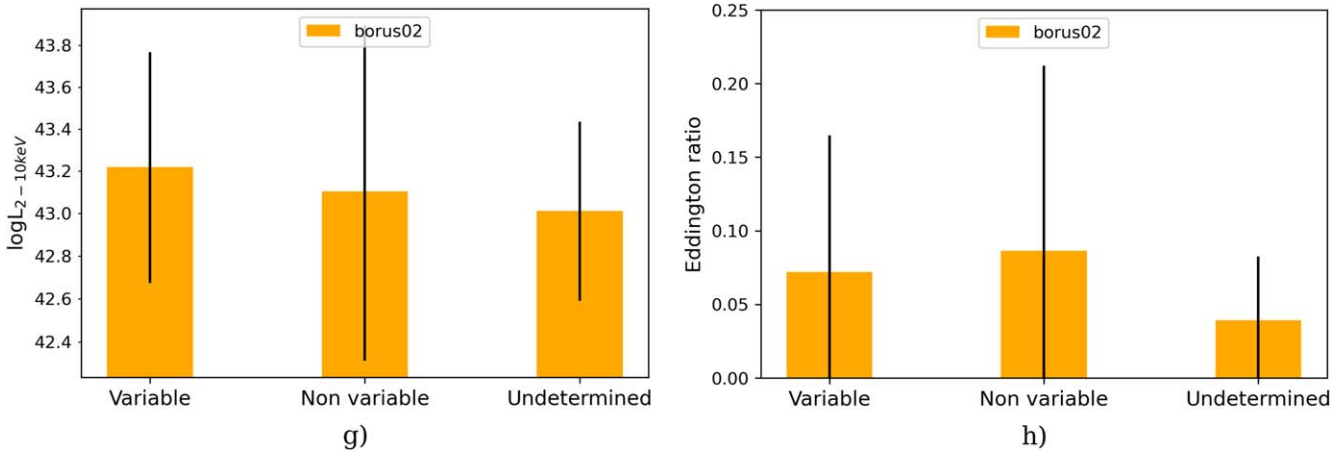

Figure 4. Bar plots displaying the averaged best-fit values for all sources, binned by variability class. The average of each parameter is computed across the sources within each variability class, with the error bar representing the standard deviation of each distribution. The models are color-coded as follows: yellow for `borus02`, magenta for `MYTorus`, and violet for `UXCLUMPY`. g) Logarithm of the intrinsic luminosity of the first NuSTAR observation in the 2–10 keV regime. We report only `borus02` measurements for clarity. h) Eddington ratio calculated by applying the bolometric correction reported in R. V. Vasudevan et al. (2010) to the $L_{2-10\ \mathrm{keV}}$ measured by `borus02`, and using the black hole masses as reported in M. J. Koss et al. (2022).

J. A. Braatz & N. E. Gugliucci (2008), and IRAS 16288+3929 L. J. Greenhill et al. (2009); Megamaser Cosmology Project[18]. On the other hand, NGC 4388 hosts a 22 GHz maser disk (J. A. Braatz et al. 2004) but does not require the inner reflector to fit the spectra.[19] The partial discrepancy in the correlation between the presence of the inner reflector and the water megamaser disk could be attributed to several factors: first, the need for an almost perfectly edge-on geometry to produce maser amplification, which may not always align with the AGN studied here, where characterizing the torus inclination angle proves highly degenerate. Second, as shown in F. Panessa & M. Giroletti (2013), there exists an observational bias in terms of distance, with the detection fraction of water megamasers being approximately 26% in a sample of Seyfert galaxies located within 20 Mpc, implying that some of the more distant AGN requiring an inner reflector may host a megamaser disk that is too faint to be detected. Moreover, the inner reflector may be located in a dust-free region of the torus, precluding the presence of masing water molecules. Finally, not all the sources analyzed in this work have been observed in maser campaigns; thus, a targeted observing campaign would benefit the understanding of the possible connection between the inner ring and the water megamaser disk.

5.2.4. $N_{H,los}$ Variations as Function of Time

In the top panel of Figure 5, we present the variations in $N_{\mathrm{H,los}}$ observed between any pair of available observations for each source, plotted against the time interval between the two observations. Since all three models are compatible with each other, we only show the results obtained with `borus02`. For reference, we provide the position where the obscuring material would be located to induce an eclipse within that timeframe, following the approach proposed by G. Risaliti et al. (2005). As shown in the figure, minor variations in $N_{\mathrm{H,los}}$ are evident across all time intervals between observations. However, significant fluctuations in $N_{\mathrm{H,los}}$ ($\Delta N_{\mathrm{H,los}} > 50 \times 10^{22}\ \mathrm{cm}^{-2}$) are more probable with larger time intervals (>100 days). This could be interpreted as a consequence of the heterogeneity and

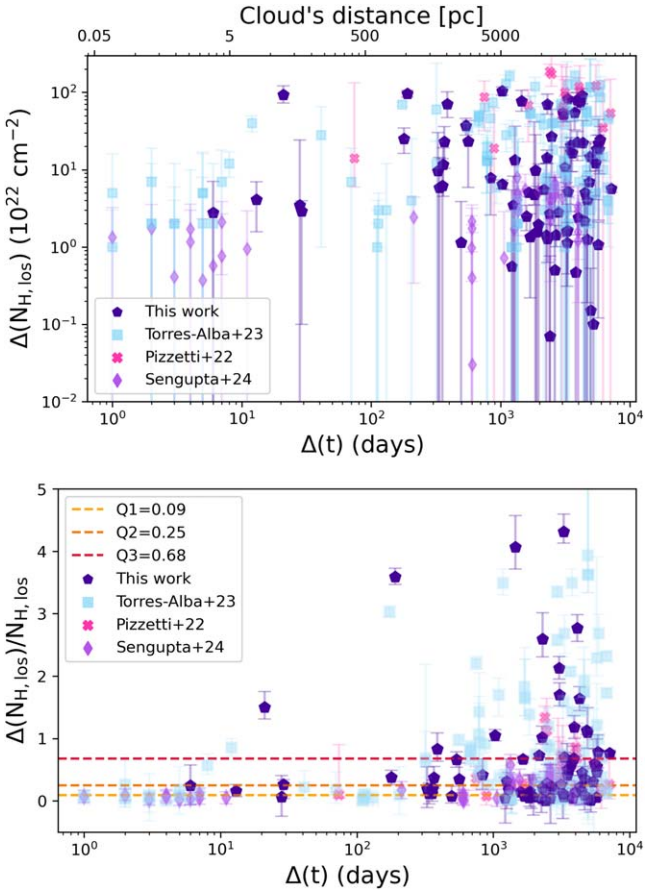

Figure 5. Top panel: Variation in $N_{\mathrm{H,los}}$ between all pairs of observations for each source relative to the time span between the two observations. The upper x-axis serves as a reference to indicate the position where the obscuring material would be located to induce an eclipse within that timeframe, following the approach proposed by G. Risaliti et al. (2005). In this approach, we note that the cloud's distance is computed by assuming the observed $\Delta N_{\mathrm{H,los}}$ is generated by a single cloud eclipsing event, which is not necessarily the case. Bottom panel: Fractional fluctuation of $N_{\mathrm{H,los}}$ between two observations of the same source, normalized to the lowest $N_{\mathrm{H,los}}$ measure in each pair. The 25%, 50%, and 75% quartiles of the distribution, (respectively, Q1, Q2, and Q3) are shown as dashed horizontal lines.

[18] https://safe.nrao.edu/wiki/bin/view/Main/PublicWaterMaserList

[19] We note the fit does not firmly rule out the presence of the component.

dimensions of the single clouds, as proposed by NTA23. However, it is important to note that this study is biased toward longer timescales. The observations analyzed in this work were not part of monitoring campaigns but were conducted randomly over the years (e.g., to monitor supernova explosions, ultraluminous X-ray sources, and star-forming regions within the galaxies). Therefore, only dedicated campaigns designed to monitor $N_{\rm H,los}$ variability can accurately populate the plot (see, e.g., the dedicated monitoring campaign for NGC 1358 in S. Marchesi et al. 2022).

The lower panel of Figure 5 presents the $N_{\rm H,los}$ variation between two observations (of each source) normalized to the lowest $N_{\rm H,los}$ value in each pair. The 25%, 50%, and 75% quartiles of the distribution are also provided, demonstrating that when randomly selecting two observations of the same source, the median variability between the two is 25% of the lower $N_{\rm H,los}$ value. For a quarter of the observation pairs in the sample, the increase is above 70%. The results differ from those reported by NTA23, who obtained higher quantiles, suggesting that, on average, the combined sample exhibits smaller variations in $N_{\rm H,los}$.

6. Conclusions

This work presents the simultaneous multiepoch analysis of 13 likely variable Compton-thin galaxies selected from a sample of heavily obscured AGN previously analyzed by XZ21. Each source has been analyzed using three torus models, i.e., `borus02`, `MYTorus`, and `UXCLUMPY`, yielding insights into geometrical properties such as the covering factor and cloud dispersion, as well as the photon index and average hydrogen column density, among other parameters. The line-of-sight hydrogen column density was determined for each source at each epoch, allowing for the categorization of each galaxy into "$N_{\rm H,los}$-Variable," "Nonvariable in $N_{\rm H,los}$" or "Undetermined," depending on the estimated degree of variability. We then discussed the $N_{\rm H,los}$ variability properties of the full sample of 27 galaxies—13 analyzed in this work, 12 in NTA23, one in A. Pizzetti et al. (2022), and one D. Sengupta et al. (2024). We summarize here our conclusions:

1. In total, 37% of the sources (10 out of 27) exhibit $N_{\rm H,los}$ variability, indicating that variations in $N_{\rm H,los}$ are necessary to achieve a proper fit across the available observations. For 44% of the sources (12 out of 27), we can confidently say that no $N_{\rm H,los}$ variability is required over the analyzed timeframe. However, all sources necessitate either flux or $N_{\rm H,los}$ (or both) variability, aligning with the anticipated outcomes based on the sample selection criteria.
2. By comparing the torus geometrical and intrinsic properties among the three classes of variability, it becomes evident that, within errors, there appears to be no distinction between the "Variable," "Nonvariable," and "Undetermined" sources, suggesting that there are no intrinsic differences between the variable and nonvariable sources considered in this study.
3. For 85% of the total sample (23 out of 27), we measured a difference between the $N_{\rm H,los}$ and $N_{\rm H,av}$ in support of the clumpy torus scenario; this implies the potential disconnection of the material responsible for reflection and absorption, as suggested by NTA23. For 12 out of 27 sources, the clouds ($N_{\rm H,los}$) are denser than the average density of the torus ($N_{\rm H,av}$), suggesting a scenario in which overdense clouds are dispersed in a less dense intercloud medium, acting as a thin-reflector. For 9 out of 27 sources, the average density of the torus is found to be denser than the clouds, indicating the presence of a geometrically thin (i.e., warped disk), dense reflector. Two sources exhibit characteristics aligning with both scenarios, depending on the considered model.
4. In total, 48% (13 out of 27) of the analyzed sources require the inclusion of a CT reflector (inner ring) in the fitting process with `UXCLUMPY`. Among these, four exhibit recorded 22 GHz water megamaser emission, suggesting a potential shared nature and spatial properties between the inner reflector and the megamaser disk. The partial discrepancy in the correlation between the presence of the inner reflector and the water megamaser disk is also discussed.
5. The median variation in $N_{\rm H,los}$ between any two observations of the same source is of 25% with respect to the lowest $N_{\rm H,los}$ value in the pair. This value is less than what was previously reported in NTA23, where the median variation was 36%, indicating that, on average, the entire sample displays smaller variations in $N_{\rm H,los}$. In a quarter of the observation pairs in the sample, the fractional difference in $N_{\rm H,los}$ between two observations exceeds 70%.
6. We present the equatorial hydrogen column density as computed for the `UXCLUMPY` model and provide an open-source tool to compute the $N_{\rm H,eq}$ from CTKcover and TORσ obtained from spectral fitting.

Acknowledgments

A.P., N.T., I.C., and M.A. acknowledge funding from NASA (contracts 80NSSC23K1611, 80NSSC23K0484, 80NSSC23K0146). The scientific results reported in this article are based on observations made by the X-ray observatories NuSTAR, XMM-Newton, and Chandra. This research has made use of the NuSTAR Data Analysis Software (NuSTARDAS) jointly developed by the ASI Space Science Data Center (SSDC, Italy) and the California Institute of Technology (Caltech, USA), and the NASA/IPAC Extragalactic Database (NED), operated by the Jet Propulsion Laboratory, California Institute of Technology, under contract with NASA. We acknowledge the use of the software packages XMM-SAS and HEASoft.

This paper employs a list of Chandra data sets, obtained by the Chandra X-ray Observatory, contained in the Chandra Data Collection (CDC) 303 and available via DOI:10.25574/cdc.303.

Software: CIAO (v4.14, A. Fruscione et al. 2006), XSPEC (K. A. Arnaud 1996), HEAsoft, SAS (C. Gabriel et al. 2004).

Appendix A
X-Ray Fitting Results

The best-fit values of the simultaneous multiepoch analysis of the sources analyzed in this work are listed in Tables 5–16.

Table 5
X-Ray Fitting Results for NGC 454E

Parameter		borus02	MYTorus dec	UXCLUMPY
stat/d.o.f		973.14/859	944.00/857	⋯
red stat		1.13	1.10	⋯
T		3.89	2.97	⋯
p-value		6.13×10^{-16}	1.95×10^{-19}	⋯
kT		$0.67^{+0.08}_{-0.11}$	$0.68^{+0.08}_{-0.10}$	⋯
apec norm ($\times 10^{-6}$)		$3.20^{+0.80}_{-0.43}$	$3.43^{+0.83}_{-0.83}$	⋯
Γ		$1.65^{+0.04}_{-0.05}$	$1.66^{+0.04}_{-0.04}$	⋯
$N_{H,av} \times 10^{24}$ cm^{-2}		$0.056^{+0.005}_{-0.007}$	$0.11^{+0.02}_{-0.01}$	⋯
C_F		$0.75^{+0.11}_{-0.07}$	…	⋯
$\cos(\theta_i)$		<0.33	…	⋯
θ_i		…	…	⋯
CTKcover		…	…	⋯
TORσ		…	…	⋯
$A_{S,90}$		…	$0.38^{+0.13}_{-0.08}$	⋯
$A_{S,0}$		…	$1.55^{+0.21}_{-0.19}$	⋯
$F_s(\times 10^{-3})$		$14.39^{+3.26}_{-4.38}$	$14.05^{+4.36}_{-3.37}$	⋯
Norm (10^{-3})		$1.84^{+0.67}_{-0.39}$	$2.00^{+0.41}_{-0.49}$	⋯
C_{AGN}	Suzaku	$1.64^{+0.43}_{-0.43}$	$1.48^{+0.45}_{-0.29}$	⋯
	XMM-Newton	$0.78^{+0.19}_{-0.20}$	$0.72^{+0.21}_{-0.14}$	⋯
	Chandra - 1	$0.66^{+0.23}_{-0.20}$	$0.62^{+0.25}_{-0.17}$	⋯
	NuSTAR - 1	1	1	⋯
	NuSTAR - 2	$0.70^{+0.20}_{-0.21}$	$0.63^{+0.21}_{-0.15}$	⋯
	Chandra - 2	=NuSTAR - 2	=NuSTAR - 2	⋯
$N_{H,los} \times 10^{22}$ cm^{-2}	Suzaku	$123.13^{+8.71}_{-7.86}$	$136.07^{+16.68}_{-11.98}$	⋯
	XMM-Newton	$26.82^{+1.43}_{-1.34}$	$26.66^{+1.45}_{-1.39}$	⋯
	Chandra - 1	$19.02^{+4.62}_{-3.87}$	$19.00^{+4.69}_{-3.91}$	⋯
	NuSTAR - 1	$96.32^{+24.59}_{-16.16}$	$109.81^{+25.06}_{-23.07}$	⋯
	NuSTAR - 2	$101.07^{+12.36}_{-14.93}$	$104.29^{+15.70}_{-14.61}$	⋯
	Chandra - 2	=NuSTAR - 2	= NuSTAR - 2	⋯
log $L_{NuSTAR,2-10\ keV}$		$42.38^{+0.04}_{-0.09}$	$42.43^{+0.11}_{-0.12}$	⋯
log $L_{NuSTAR,10-40\ keV}$		$42.02^{+0.05}_{-0.06}$	$41.87^{+0.06}_{-0.06}$	⋯
Red stat - No Var.		3.87	3.70	⋯
T		84.62	79.62	⋯
Red stat - No C_{AGN}Var.		1.80	1.73	⋯
T		23.74	21.61	⋯
Red stat - No $N_{H,los}$ Var.		3.08	2.94	⋯
T		61.21	57.06	⋯

Note. Same as Table 2.

Table 6
X-Ray Fitting Results for MRK 348

Parameter		borus02	MYTorus dec	UXCLUMPY
χ^2/d.o.f		3978.12/3168	3820.06/3170	3983.08/3172
red χ^2		1.25	1.20	1.25
T		14.39	11.54	14.40
p-value		4.43×10^{-55}	5.31×10^{-319}	6.01×10^{-59}
kT		$0.78^{+0.04}_{-0.05}$	$0.78^{+0.03}_{-0.04}$	$0.79^{+0.05}_{-0.05}$
	XMM-Newton - 1	< 0.84	$5.41^{+1.90}_{-1.92}$	= XMM - 2
apec norm($\times 10^{-6}$)	XMM-Newton - 2	$16.22^{+2.24}_{-2.23}$	$18.29^{+2.23}_{-2.22}$	$15.95^{+2.22}_{-2.24}$
	Suzaku	$21.34^{+2.07}_{-2.09}$	$27.93^{+2.07}_{-2.07}$	$20.62^{+2.06}_{-2.24}$
Γ		$1.51^{+0.02}_{-0.01}$	$1.61^{+0.01}_{-0.01}$	$1.69^{+0.01}_{-0.01}$
$N_{\rm H,av} \times 10^{24}$ cm^{-2}		$0.22^{+0.10}_{-0.03}$	$0.30^{+0.02}_{-0.02}$	…
C_F		$0.38^{+0.04}_{-0.07}$	…	…
$\cos(\theta_i)$		$0.35^{+0.02}_{-0.07}$	…	…
θ_i		…	…	70^{*}
CTKcover		…	…	0^{*}
TORσ		…	…	$27.99^{+2.58}_{-0.59}$
$A_{S,90}$		…	$0.14^{+0.02}_{-0.02}$	…
$A_{S,0}$		…	$4.68^{+0.48}_{-0.42}$	…
$F_s(\times 10^{-3})$		$5.67^{+0.29}_{-0.32}$	$2.92^{+0.50}_{-0.61}$	$14.61^{+0.82}_{-1.70}$
Norm (10^{-3})		$9.72^{+0.29}_{-0.26}$	$10.39^{+0.31}_{-0.30}$	$18.77^{+0.65}_{-0.72}$
	XMM-Newton - 1	$1.16^{+0.02}_{-0.02}$	$1.09^{+0.02}_{-0.02}$	$1.06^{+0.03}_{-0.02}$
	Suzaku	$1.06^{+0.01}_{-0.01}$	$1.02^{+0.01}_{-0.01}$	$0.99^{+0.02}_{-0.02}$
$C_{\rm AGN}$	XMM-Newton - 2	$0.33^{+0.01}_{-0.01}$	$0.31^{+0.01}_{-0.01}$	$0.30^{+0.01}_{-0.01}$
	NuSTAR - 1	1	1	1
	NuSTAR - 2	$0.90^{+0.01}_{-0.01}$	$0.85^{+0.01}_{-0.01}$	$0.86^{+0.01}_{-0.01}$
	XMM-Newton -1	$13.08^{+0.20}_{-0.24}$	$13.50^{+0.27}_{-0.24}$	$12.73^{+0.17}_{-0.17}$
	Suzaku	$7.58^{+0.07}_{-0.07}$	$7.46^{+0.08}_{-0.07}$	$7.52^{+0.08}_{-0.08}$
$N_{\rm H,los} \times 10^{22}$ cm^{-2}	XMM-Newton - 2	$12.61^{+0.51}_{-0.48}$	$12.91^{+0.62}_{-0.56}$	$12.30^{+0.42}_{-0.42}$
	NuSTAR - 1	$6.16^{+0.41}_{-0.34}$	$5.74^{+0.41}_{-0.40}$	$6.72^{+0.34}_{-0.35}$
	NuSTAR - 2	$7.43^{+0.31}_{-0.30}$	$7.13^{+0.34}_{-0.32}$	$7.52^{+0.27}_{-0.28}$
log $L_{\rm NuSTAR,2-10\ keV}$		$43.42^{+0.04}_{-0.05}$	$43.374^{+0.008}_{-0.008}$	43.58
log $L_{\rm NuSTAR,10-40\ keV}$		$43.59^{+0.04}_{-0.05}$	$43.204^{+0.007}_{-0.007}$	43.69
Red stat - No Var.		19.50	19.78	19.85
T		1042.74	1058.92	1063.43
Red stat - No $C_{\rm AGN}$Var.		1.83	1.63	2.02
T		47.20	35.83	57.69
Red stat - No $N_{\rm H,los}$ Var.		2.32	2.29	2.80
T		74.57	72.87	101.78

Note. Same as Table 2. $\theta_{i,\rm uxclumpy} = \arccos(\cos(\theta_{i,\rm borus02}))$. CTKcover is frozen because it is compatible with the hard limit of the available range.

Table 7
X-Ray Fitting Results for NGC 4992

Parameter		borus02	MYTorus dec	UXCLUMPY
stat/d.o.f		529.95/530	538.43/532	543.71/530
red stat		0.99	1.01	1.02
T		0.002	0.30	0.60
p-value		0.58	0.38	0.74
kT		$0.23^{+0.04}_{-0.03}$	$0.24^{+0.03}_{-0.03}$	$0.24^{+0.04}_{-0.03}$
apec norm($\times 10^{-4}$)		$0.92^{+0.46}_{-0.29}$	$0.91^{+0.45}_{-0.28}$	$0.85^{+0.43}_{-0.25}$
Γ		$1.68^{+0.09}_{-0.12}$	$1.68^{+0.06}_{-0.07}$	$1.66^{+0.11}_{-0.06}$
$N_{\rm H,av} \times 10^{24}$ cm^{-2}		$1.86^{+0.48}_{-0.34}$	$2.00^{+0.53}_{-0.32}$	…
C_F		$0.67^{+0.12}_{-0.20}$	…	…
cos(θ_i)		$0.59^{+0.55}_{-0.16}$	…	…
θ_i		…	…	> 26.19
CTKcover		…	…	< 0.30
TORσ		…	…	$28.18^{+18.32}_{-4.11}$
$A_{S,90}$		…	$0.85^{+0.69}_{-0.27}$	…
$A_{S,0}$		…	$0.71^{+0.35}_{-0.37}$	…
$F_s(\times 10^{-3})$		$4.00^{+1.85}_{-1.14}$	$3.37^{+1.26}_{-0.95}$	$10.73^{+10.38}_{-6.39}$
Norm (10^{-3})		$3.34^{+0.90}_{-0.81}$	$6.63^{+0.83}_{-0.70}$	$4.36^{+2.00}_{-1.39}$
$C_{\rm AGN}$	Chandra - a	$1.09^{+0.51}_{-0.37}$	$1.11^{+0.55}_{-0.39}$	$1.04^{+0.56}_{-0.34}$
	Suzaku	$1.12^{+0.12}_{-0.13}$	$1.17^{+0.15}_{-0.13}$	$1.14^{+0.19}_{-0.12}$
	XMM-Newton	$1.06^{+0.08}_{-0.14}$	$1.08^{+0.16}_{-0.14}$	$1.01^{+0.18}_{-0.15}$
	NuSTAR	1	1	1
	Chandra - b	$0.92^{+0.24}_{-0.20}$	$0.92^{+0.26}_{-0.20}$	$0.89^{+0.21}_{-0.17}$
$N_{\rm H,los} \times 10^{22}$ cm^{-2}	Chandra - a	$61.74^{+16.80}_{-14.17}$	$64.03^{+17.79}_{-15.03}$	$63.98^{+22.90}_{-14.88}$
	Suzaku	$52.04^{+3.68}_{-2.65}$	$54.72^{+2.85}_{-2.74}$	$55.06^{+9.87}_{-2.17}$
	XMM-Newton	$58.24^{+3.94}_{-4.17}$	$60.41^{+4.62}_{-4.22}$	$59.78^{+7.40}_{-4.27}$
	NuSTAR	$41.26^{+4.87}_{-3.41}$	$42.27^{+4.02}_{-4.17}$	$45.14^{+6.18}_{-7.15}$
	Chandra - b	$39.86^{+5.81}_{-5.45}$	$38.87^{+5.81}_{-5.45}$	$39.84^{+6.24}_{-4.23}$
log $L_{\rm NuSTAR,2-10\ keV}$		$43.24^{+0.01}_{-0.04}$	$43.28^{+0.07}_{-0.06}$	43.50
log $L_{\rm NuSTAR,10-40\ keV}$		$43.22^{+0.06}_{-0.06}$	$43.18^{+0.04}_{-0.05}$	43.63
Red stat - No Var.		1.08	1.31	1.29
T		2.17	7.34	6.83
Red stat - No $C_{\rm AGN}$Var.		0.99	1.02	1.03
T		0.01	0.37	0.73
Red stat - No $N_{\rm H,los}$ Var.		1.06	1.07	1.07
T		1.35	1.71	1.61

Note. Same as Table 2.

Table 8
X-Ray Fitting Results for ESO 383-18

Parameter		borus02	MYTorus dec	UXCLUMPY
stat/d.o.f		1763.60/1477	1647.21/1474	1817.30/1477
red stat		1.19	1.11	1.23
T		7.45	4.51	8.85
p-value		0.43	0.11	0.80
kT		$0.17^{+0.03}_{-0.03}$	$0.68^{+0.10}_{-0.12}$	$0.22^{+0.05}_{-0.04}$
apec norm($\times 10^{-4}$)		$0.11^{+0.08}_{-0.06}$	$0.05^{+0.01}_{-0.01}$	$0.13^{+0.06}_{-0.06}$
Γ		$1.52^{+0.03}_{-0.04}$	$1.79^{+0.03}_{-0.03}$	$1.46^{+0.03}_{-0.01}$
$N_{\rm H,av} \times 10^{24}$ cm^{-2}		$0.97^{+0.07}_{-0.10}$	$1.00^{+0.03}_{-0.05}$	…
C_F		$0.55^{+0.02}_{-0.12}$	…	…
$\cos(\theta_i)$		<0.29	…	…
θ_i		…	…	$64.55^{+16.59}_{-8.56}$
CTKcover		…	…	0*
TORσ		…	…	$7.90^{+3.58}_{-1.17}$
$A_{S,90}$		…	$0.06^{+0.02}_{-0.02}$	…
$A_{S,0}$		…	$7.65^{+0.91}_{-1.08}$	…
$F_s(\times 10^{-3})$		$8.90^{+1.10}_{-1.31}$	$2.42^{+1.04}_{-1.10}$	$12.37^{+0.98}_{-0.98}$
Norm (10^{-3})		$2.16^{+0.16}_{-0.24}$	$2.26^{+0.17}_{-0.17}$	$2.63^{+0.31}_{-0.30}$
$C_{\rm AGN}$	XMM-Newton	$1.27^{+0.06}_{-0.04}$	$1.35^{+0.06}_{-0.07}$	$1.24^{+0.06}_{-0.05}$
	NuSTAR-1	1	1	1
	NuSTAR-2	$0.93^{+0.02}_{-0.02}$	$0.92^{+0.03}_{-0.03}$	$0.91^{+0.04}_{-0.02}$
	Chandra	$0.42^{+0.08}_{-0.10}$	$0.44^{+0.32}_{-0.14}$	$0.41^{+0.21}_{-0.14}$
$N_{\rm H,los} \times 10^{22}$ cm^{-2}	XMM-Newton	$18.82^{+0.94}_{-0.43}$	$19.95^{+0.88}_{-0.95}$	$17.76^{+0.68}_{-0.71}$
	NuSTAR-1	$16.03^{+1.76}_{-1.01}$	$13.79^{+1.65}_{-1.53}$	$14.79^{+1.51}_{-1.38}$
	NuSTAR-2	$17.17^{+0.99}_{-0.77}$	$15.14^{+0.91}_{-0.95}$	$16.06^{+0.96}_{-0.94}$
	Chandra	$18.72^{+3.56}_{-3.03}$	$19.95^{+5.69}_{-4.17}$	$17.61^{+4.48}_{-3.61}$
log $L_{\rm NuSTAR,2-10\ keV}$		$42.58^{+0.03}_{-0.01}$	$42.46^{+0.03}_{-0.03}$	42.69
log $L_{\rm NuSTAR,10-40\ keV}$		$42.74^{+0.02}_{-0.02}$	$41.81^{+0.05}_{-0.05}$	42.95
Red stat - No Var.		1.31	1.38	1.49
T		12.18	14.79	18.94
Red stat - No $C_{\rm AGN}$Var.		1.24	1.25	1.35
T		9.36	9.88	13.43
Red stat - No $N_{\rm H,los}$ Var.		1.23	1.18	1.23
T		9.04	7.18	9.11

Note. Same as Table 2.

Table 9
X-Ray Fitting Results for MRK 417

Parameter		borus02	MYTorus dec	UXCLUMPY
stat/d.o.f		571.20/550	568.64/552	564.47/552
red stat		1.04	1.03	1.02
T		0.90	0.71	0.53
p-value		0.07	0.11	0.07
kT		$0.79^{+0.08}_{-0.09}$	$0.79^{+0.08}_{-0.09}$	$0.79^{+0.08}_{-0.10}$
apec norm($\times 10^{-4}$)		$0.07^{+0.02}_{-0.02}$	$0.07^{+0.02}_{-0.01}$	$0.06^{+0.02}_{-0.02}$
Γ		$1.53^{+0.06}_{-0.07}$	$1.64^{+0.07}_{-0.09}$	$1.64^{+0.11}_{-0.08}$
$N_{\rm H,av} \times 10^{24}$ cm^{-2}		$0.12^{+0.06}_{-0.03}$	$0.69^{+0.32}_{-0.25}$	…
C_F		$0.44^{+0.12}_{-0.12}$	…	…
$\cos(\theta_i)$		<0.37	…	…
θ_i		…	…	$56.06^{+10.45}_{-16.60}$
CTKcover		…	…	0*
TORσ		…	…	$9.39^{+6.77}_{-2.92}$
$A_{S,90}$		…	$0.22^{+1.04}_{-0.06}$	…
$A_{S,0}$		…	$1.93^{+0.87}_{-1.60}$	…
$F_s(\times 10^{-3})$		$9.53^{+3.11}_{-1.66}$	$9.20^{+3.03}_{-2.39}$	$14.34^{+7.28}_{-8.12}$
Norm (10^{-3})		$2.11^{+0.43}_{-0.42}$	$2.13^{+0.42}_{-0.42}$	$3.14^{+1.27}_{-0.63}$
$C_{\rm AGN}$	XMM-Newton	$0.74^{+0.15}_{-0.12}$	$0.70^{+0.12}_{-0.11}$	$0.54^{+0.11}_{-0.06}$
	Suzaku	$1.54^{+0.18}_{-0.20}$	$1.47^{+0.22}_{-0.17}$	$1.26^{+0.12}_{-0.14}$
	NuSTAR	1	1	1
	Chandra	$0.80^{+0.25}_{-0.18}$	$0.81^{+0.22}_{-0.17}$	$0.78^{+0.20}_{-0.16}$
$N_{\rm H,los} \times 10^{22}$ cm^{-2}	XMM-Newton	$55.18^{+5.43}_{-5.34}$	$55.10^{+7.58}_{-6.40}$	$56.22^{+4.82}_{-4.79}$
	Suzaku	$49.33^{+3.13}_{-3.20}$	$47.56^{+5.69}_{-3.85}$	$44.00^{+2.30}_{-2.22}$
	NuSTAR	$32.90^{+3.44}_{-3.80}$	$30.38^{+3.92}_{-3.32}$	$30.48^{+5.01}_{-3.94}$
	Chandra	$30.95^{+6.50}_{-5.57}$	$29.23^{+6.48}_{-5.21}$	$27.99^{+5.72}_{-4.73}$
log $L_{\rm NuSTAR,2-10\ keV}$		$43.42^{+0.08}_{-0.08}$	$43.32^{+0.08}_{-0.07}$	43.50
log $L_{\rm NuSTAR,10-40\ keV}$		$43.48^{+0.03}_{-0.04}$	$42.25^{+0.09}_{-0.07}$	43.65
Red stat - No Var.		2.58	2.58	2.57
T		37.23	37.29	37.06
Red stat - No $C_{\rm AGN}$Var.		1.22	1.23	1.21
T		5.11	5.57	4.98
Red stat - No $N_{\rm H,los}$ Var.		1.11	1.10	1.10
T		2.64	2.57	2.57

Note. Same as Table 2.

Table 10
X-Ray Fitting Results for MCG-01-05-047

Parameter		borus02	MYTorus dec	UXCLUMPY
χ^2/d.o.f		624.05/529	565.25/531	642.27/530
red χ^2		1.18	1.06	1.21
T		4.13	1.48	4.87
p-value		0.003	3.01×10^{-274}	0.046
kT		…	…	…
apec norm		…	…	…
Γ		$1.61^{+0.15}_{-0.03}$	$1.66^{+0.18}_{-0.15}$	$1.37^{+0.07}_{-0.11}$
$N_{\rm H,av} \times 10^{24}$ cm^{-2}		>1.41	$0.21^{+0.05}_{-0.03}$	…
C_F		$0.69^{+0.01}_{-0.40}$	…	…
$\cos(\theta_i)$		$0.75^{+0.04}_{-0.18}$	…	…
θ_i		…	…	0*
CTKcover		…	…	>0.21
TORσ		…	…	$27.23^{+16.78}_{-2.52}$
$A_{S,90}$		…	$0.15^{+0.03}_{-0.03}$	…
$A_{S,0}$		…	$4.77^{+2.22}_{-1.96}$	…
$F_s(\times 10^{-3})$		$19.61^{+8.64}_{-9.76}$	$3.55^{+2.92}_{-3.47}$	>31.83
Norm (10^{-3})		$1.08^{+0.52}_{-0.10}$	$4.81^{+1.32}_{-0.88}$	$0.80^{+0.21}_{-0.23}$
$C_{\rm AGN}$	Suzaku	$0.75^{+0.10}_{-0.10}$	$0.84^{+0.05}_{-0.05}$	$0.86^{+0.12}_{-0.08}$
	XMM-Newton	$1.47^{+0.20}_{-0.20}$	$0.35^{+0.04}_{-0.04}$	$1.72^{+0.22}_{-0.16}$
	NuSTAR	1	1	1
	Chandra	$1.86^{+0.33}_{-0.30}$	$0.46^{+0.11}_{-0.06}$	$2.20^{+0.41}_{-0.26}$
$N_{\rm H,los} \times 10^{22}$ cm^{-2}	Suzaku	$11.24^{+0.46}_{-1.36}$	>188.52	$9.13^{+0.63}_{-0.72}$
	XMM-Newton	$14.15^{+0.60}_{-1.45}$	$15.39^{+1.85}_{-1.55}$	$12.24^{+1.11}_{-1.36}$
	NuSTAR	$14.71^{+4.28}_{-4.24}$	$234.25^{+53.58}_{-42.94}$	$9.68^{+2.59}_{-1.73}$
	Chandra	$16.30^{+0.97}_{-1.78}$	$18.66^{+3.12}_{-2.31}$	$14.14^{+2.00}_{-0.84}$
log $L_{\rm NuSTAR,2-10\ keV}$		$42.53^{+0.06}_{-0.08}$	$43.14^{+0.29}_{-0.17}$	42.54
log log $L_{\rm NuSTAR,10-40\ keV}$		$42.29^{+0.05}_{-0.06}$	$41.87^{+0.12}_{-0.06}$	42.85
Red stat - No Var.		2.63	2.13	2.12
T		37.72	26.24	26.00
Red stat - No $C_{\rm AGN}$Var.		1.79	1.31	1.62
T		18.33	7.28	14.43
Red stat - No $N_{\rm H,los}$ Var.		1.42	1.37	1.27
T		9.84	8.62	6.32

Note. Same as Table 2. UXCLUMPY angle θ_i is frozen because it is compatible with the hard limit of the available range.

Table 11
X-Ray Fitting Results for ESO 103-35

Parameter		borus02	MYTorus dec	UXCLUMPY
χ^2/d.o.f		3961.46/3868	3926.45/3869	3947.50/3870
red χ^2		1.02	1.01	1.02
T		0.92	1.50	1.24
p-value		0.07	0.06	0.02
kT		$0.73^{+0.04}_{-0.05}$	$0.74^{+0.04}_{-0.04}$	$0.73^{+0.04}_{-0.05}$
apec norm($\times 10^{-4}$)	XMM-Newton	$0.03^{+0.02}_{-0.02}$	$0.07^{+0.02}_{-0.02}$	$0.03^{+0.02}_{-0.02}$
	Suzaku	$0.33^{+0.03}_{-0.03}$	$0.37^{+0.02}_{-0.03}$	$0.33^{+0.03}_{-0.03}$
Γ		$1.81^{+0.02}_{-0.01}$	$1.95^{+0.02}_{-0.02}$	$1.81^{+0.03}_{-0.02}$
$N_{H,av} \times 10^{24}$ cm^{-2}		$2.13^{+0.29}_{-0.28}$	$0.60^{+0.29}_{-0.21}$	…
C_F		$0.56^{+0.02}_{-0.03}$	…	…
$\cos(\theta_i)$		$0.49^{+0.02}_{-0.02}$	…	…
θ_i		…	…	$79.81^{+8.30}_{-10.73}$
CTKcover		…	…	$0.34^{+0.05}_{-0.03}$
TORσ		…	…	>81.83
$A_{S,90}$		…	$0.30^{+0.04}_{-0.03}$	…
$A_{S,0}$		…	$1.67^{+0.14}_{-0.12}$	…
$F_s(\times 10^{-3})$		$1.06^{+0.26}_{-0.19}$	<0.10	$10.07^{+4.66}_{-16.373}$
Norm (10^{-3})		$14.20^{+0.81}_{-0.55}$	$17.75^{+1.29}_{-1.21}$	$18.03^{+0.11}_{-0.85}$
C_{AGN}	XMM-Newton	$1.37^{+0.04}_{-0.04}$	$1.37^{+0.04}_{-0.04}$	$1.39^{+0.04}_{-0.04}$
	Suzaku	$1.42^{+0.03}_{-0.03}$	$1.43^{+0.03}_{-0.03}$	$1.44^{+0.04}_{-0.03}$
	NuSTAR 1	1	1	1
	NuSTAR 2	$1.02^{+0.02}_{-0.02}$	$1.01^{+0.02}_{-0.02}$	$1.02^{+0.02}_{-0.02}$
$N_{H,los} \times 10^{22}$ cm^{-2}	XMM-Newton	$19.97^{+0.40}_{-0.39}$	$20.84^{+0.46}_{-0.44}$	$18.84^{+0.31}_{-0.32}$
	Suzaku	$20.04^{+0.29}_{-0.27}$	$20.91^{+0.35}_{-0.34}$	$18.76^{+0.22}_{-0.21}$
	NuSTAR 1	$17.56^{+0.69}_{-0.58}$	$18.04^{+0.73}_{-0.67}$	$16.37^{+0.59}_{-0.61}$
	NuSTAR 2	$18.91^{+0.65}_{-0.55}$	$19.39^{+0.70}_{-0.64}$	$17.62^{+0.52}_{-0.54}$
log $L_{NuSTAR,2-10\ keV}$		$43.26^{+0.001}_{-0.001}$	$43.41^{+0.01}_{-0.02}$	43.47
log $L_{NuSTAR,10-40\ keV}$		$43.20^{+0.01}_{-0.01}$	$43.01^{+0.01}_{-0.01}$	43.38
Red stat - No Var.		1.56	1.63	1.65
T		34.96	39.25	40.76
Red stat - No C_{AGN}Var.		1.17	1.17	1.19
T		10.80	10.88	12.18
Red stat - No $N_{H,los}$ Var.		1.08	1.03	1.09
T		4.94	1.80	5.58

Note. Same as Table 2.

Table 12
X-Ray Fitting Results for NGC 1142

Parameter		borus02	MYTorus dec	UXCLUMPY
χ^2/d.o.f		724.33/680	720.40/680	723.91/680
red χ^2		1.06	1.06	1.06
T		1.69	1.55	1.68
p-value		1.04×10^{-9}	1.28×10^{-15}	7.88×10^{-45}
kT		$0.75^{+0.03}_{-0.03}$	$0.75^{+0.03}_{-0.03}$	$0.76^{+0.04}_{-0.03}$
apec norm($\times 10^{-4}$)	XMM-Newton	$0.11^{+0.02}_{-0.02}$	$0.11^{+0.02}_{-0.02}$	$0.09^{+0.01}_{-0.02}$
	Suzaku–1	$0.27^{+0.02}_{-0.02}$	$0.27^{+0.02}_{-0.02}$	$0.26^{+0.02}_{-0.02}$
	Suzaku–2	$0.24^{+0.03}_{-0.03}$	$0.25^{+0.03}_{-0.03}$	$0.23^{+0.04}_{-0.03}$
Γ		$1.64^{+0.08}_{-0.08}$	$1.65^{+0.09}_{-0.05}$	$2.08^{+0.07}_{-0.15}$
$N_{\rm H,av} \times 10^{24}$ cm^{-2}		$0.29^{+0.03}_{-0.02}$	$0.22^{+0.02}_{-0.01}$	…
C_F		$0.40^{+0.03}_{-0.05}$	…	…
$\cos(\theta_i)$		<0.22	…	…
θ_i		…	…	>77.29
CTKcover		…	…	<0.26
TORσ		…	…	$25.71^{+31.17}_{-8.10}$
$A_{S,90}$		…	$1.09^{+0.08}_{-0.18}$	…
$A_{S,0}$		…	<0.15	…
$F_s(\times 10^{-3})$		$5.29^{+1.14}_{-0.99}$	$3.72^{+1.17}_{-0.88}$	$6.96^{+13.08}_{-4.39}$
Norm (10^{-3})		$4.08^{+1.37}_{-0.86}$	$4.55^{+1.51}_{-1.11}$	$16.70^{+4.17}_{-2.97}$
$C_{\rm AGN}$	XMM-Newton	$1.15^{+0.19}_{-0.15}$	$1.15^{+0.20}_{-0.16}$	$0.83^{+0.22}_{-0.19}$
	Suzaku–1	$1.87^{+0.28}_{-0.22}$	$1.88^{+0.30}_{-0.23}$	$1.32^{+0.36}_{-0.26}$
	Suzaku–2	$1.93^{+0.30}_{-0.23}$	$1.93^{+0.31}_{-0.24}$	$1.44^{+0.32}_{-0.27}$
	NuSTAR	1	1	1
$N_{\rm H,los} \times 10^{22}$ cm^{-2}	XMM-Newton	$55.63^{+3.83}_{-3.55}$	$56.06^{+3.16}_{-3.11}$	$56.15^{+1.95}_{-1.89}$
	Suzaku–1	$67.30^{+3.72}_{-3.58}$	$68.19^{+2.56}_{-3.08}$	$66.45^{+2.29}_{-2.74}$
	Suzaku–2	$92.42^{+5.62}_{-5.39}$	$92.16^{+5.09}_{-2.44}$	$90.90^{+5.04}_{-5.85}$
	NuSTAR	$146.84^{+15.72}_{-16.24}$	$147.22^{+11.81}_{-13.08}$	$174.37^{+27.91}_{-26.01}$
log $L_{\rm NuSTAR,2-10\ keV}$		$43.51^{+0.01}_{-0.01}$	$43.57^{+0.08}_{-0.10}$	43.82
log $L_{\rm NuSTAR,10-40\ keV}$		$42.96^{+0.07}_{-0.08}$	$43.20^{+0.06}_{-0.06}$	43.69
Red stat - No Var.		7.12	7.24	7.39
T		160.52	163.70	167.41
Red stat - No $C_{\rm AGN}$Var.		1.36	1.35	1.25
T		9.55	9.06	6.47
Red stat - No $N_{\rm H,los}$ Var.		1.36	1.35	1.38
T		9.57	9.17	10.02

Note. Same as Table 2.

Table 13
X-Ray Fitting Results for IRAS 16288+3929

Parameter		borus02	MYTorus dec	UXCLUMPY
χ^2/d.o.f		276.17/265	277.37/267	294.25/265
red χ^2		1.04	1.04	1.11
T		0.68	0.63	1.79
p-value		2.77×10^{-09}	2.02×10^{-12}	4.60×10^{-10}
kT		$0.71^{+0.07}_{-0.09}$	$0.72^{+0.07}_{-0.08}$	$0.71^{+0.07}_{-0.08}$
apec norm($\times 10^{-6}$)		$4.31^{+0.75}_{-0.75}$	$4.21^{+0.87}_{-0.93}$	$4.48^{+0.79}_{-0.85}$
Γ		$2.20^{+0.17}_{-0.08}$	$2.19^{+0.11}_{-0.11}$	$2.33^{+0.23}_{-0.14}$
$N_{\rm H,av} \times 10^{24}$ cm^{-2}		$0.29^{+0.07}_{-0.06}$	$0.29^{+0.06}_{-0.06}$	…
C_F		$0.20^{+0.37}_{-0.09}$	…	…
cos(θ_i)		0.05	…	…
θ_i		…	…	0*
CTKcover		…	…	>0.57
TORσ		…	…	$70.00^{+7.99}_{-5.94}$
$A_{S,90}$		…	$0.29^{+0.09}_{-0.12}$	…
$A_{S,0}$		…	<0.11	…
F_s($\times 10^{-3}$)		$0.007^{+0.003}_{-0.002}$	$0.82^{+0.47}_{-0.37}$	$11.57^{+14.02}_{-5.54}$
Norm (10^{-3})		$5.74^{+2.61}_{-1.92}$	$9.76^{+4.81}_{-3.17}$	$12.43^{+15.42}_{-3.92}$
$C_{\rm AGN}$	Suzaku	$5.65^{+1.03}_{-0.91}$	$5.59^{+2.08}_{-1.65}$	$4.03^{+0.78}_{-0.87}$
	XMM-Newton	$0.77^{+0.12}_{-0.12}$	$0.78^{+0.23}_{-0.18}$	$0.81^{+0.15}_{-0.28}$
	NuSTAR	1	1	1
$N_{\rm H,los} \times 10^{22}$ cm^{-2}	Suzaku	$155.61^{+22.63}_{-15.63}$	$151.73^{+19.00}_{-16.85}$	$131.18^{+13.29}_{-16.03}$
	XMM-Newton	$62.22^{+4.88}_{-4.79}$	$61.04^{+3.84}_{-3.30}$	$56.20^{+3.59}_{-1.67}$
	NuSTAR	$85.12^{+8.47}_{-7.65}$	$83.36^{+12.19}_{-10.23}$	$77.19^{+20.68}_{-7.22}$
log $L_{\rm NuSTAR,2-10\ keV}$		$43.57^{+0.13}_{-0.09}$	$43.58^{+0.14}_{-0.13}$	43.61
log $L_{\rm NuSTAR,10-40\ keV}$		$43.12^{+0.09}_{-0.48}$	$43.36^{+0.11}_{-0.11}$	43.30
Red stat - No Var.		1.58	1.62	1.59
T		9.50	10.16	9.64
Red stat - No $C_{\rm AGN}$Var.		1.36	1.36	1.32
T		5.89	5.88	5.20
Red stat - No $N_{\rm H,los}$ Var.		1.30	1.31	1.29
T		4.95	5.12	4.75

Note. Same as Table 2.

Table 14
X-Ray Fitting Results for ESO 263-13

Parameter		borus02	MYTorus dec	UXCLUMPY
χ^2/d.o.f [a]		862.24/685	859.47/686	797.37/684
red χ^2 [b]		1.31	1.25	1.16
T [c]		6.77	6.62	4.33
p-value [d]		2.87×10^{-42}	8.10×10^{-51}	6.89×10^{-89}
kT [e]		$0.78^{+0.05}_{-0.06}$	$0.78^{+0.06}_{-0.06}$	$0.78^{+0.05}_{-0.05}$
apec norm($\times 10^{-6}$) [f]		$8.98^{+1.66}_{-1.65}$	$8.74^{+1.58}_{-1.57}$	$10.42^{+1.10}_{-1.13}$
Γ [g]		$1.65^{+0.06}_{-0.06}$	$1.69^{+0.05}_{-0.05}$	$1.59^{+0.06}_{-0.08}$
$N_{H,av} \times 10^{24}$ cm^{-2} [h]		$0.09^{+0.02}_{-0.02}$	$0.08^{+0.02}_{-0.02}$	…
C_F [i]		$0.04^{+0.14}_{-0.08}$	…	…
$\cos(\theta_i)$ [j]		0.05^{u}_{u}	…	…
θ_i [k]		…	…	$44.58^{+3.68}_{-4.62}$
CTKcover [l]		…	…	$0.25^{+0.01}_{-0.02}$
TORσ [m]		…	…	$7.03^{+1.19}_{-0.22}$
$A_{S,90}$ [n]		…	$1.26^{+0.35}_{-0.32}$	…
$A_{S,0}$ [o]		…	0*	…
$F_s(\times 10^{-3})$ [p]		$9.99^{+2.79}_{-2.41}$	$9.42^{+2.82}_{-2.25}$	$15.13^{+2.10}_{-0.96}$
Norm (10^{-3}) [q]		$3.51^{+0.83}_{-0.74}$	$3.95^{+0.86}_{-0.74}$	$3.21^{+0.41}_{-0.33}$
C_{AGN} [r]	Suzaku	$1.02^{+0.16}_{-0.13}$	$1.03^{+0.15}_{-0.13}$	$1.67^{+0.32}_{-0.17}$
	XMM-Newton	$0.61^{+0.10}_{-0.08}$	$0.62^{+0.10}_{-0.08}$	$0.63^{+0.11}_{-0.11}$
	NuSTAR	1	1	1
$N_{H,los} \times 10^{22}$ cm^{-2} [s]	Suzaku	$30.09^{+1.72}_{-1.54}$	$30.80^{+1.66}_{-1.64}$	$26.85^{+0.40}_{-0.56}$
	XMM-Newton	$26.01^{+1.18}_{-0.97}$	$25.45^{+1.07}_{-1.06}$	$20.68^{+0.75}_{-0.75}$
	NuSTAR	$81.27^{+8.99}_{-8.29}$	$81.08^{+6.60}_{-8.08}$	$56.04^{+3.62}_{-2.12}$
log $L^{(t)}_{NuSTAR,2-10\ keV}$		$43.53^{+0.14}_{-0.13}$	$43.56^{+0.11}_{-0.11}$	44.22
log $L^{(u)}_{NuSTAR,10-40\ keV}$		$43.69^{+0.01}_{-0.01}$	$43.71^{+0.01}_{-0.01}$	44.39
Red stat - No Var. [v]		4.52	4.59	4.57
T		92.43	94.31	93.73v
Red stat - No C_{AGN}Var. [w]		1.42	1.49	1.41
T		11.11	12.99	10.93
Red stat - No $N_{H,los}$ Var. [x]		1.62	1.71	1.44
T		16.29	18.66	11.69

Note. Same as Table 2.

Table 15
X-Ray Fitting Results for Fairall 272

Parameter		borus02	MYTorus dec	UXCLUMPY
stat/d.o.f		590.59/616	584.99/616	593.97/617
red stat		0.96	0.95	0.96
T		0.96	0.95	0.93
p-value		3.18×10^{-4}	2.61×10^{-12}	0.01
kT		$0.75^{+0.11}_{-0.13}$	$0.79^{+0.08}_{-0.09}$	$0.77^{+0.09}_{-0.12}$
apec norm($\times 10^{-4}$)		$0.06^{+0.01}_{-0.01}$	$0.08^{+0.01}_{-0.01}$	$0.07^{+0.02}_{-0.01}$
Γ		<1.52	$1.53^{+0.11}_{-0.09}$	$1.56^{+0.04}_{-0.06}$
$N_{H,av} \times 10^{24}$ cm^{-2}		$0.65^{+0.37}_{-0.11}$	$0.74^{+0.37}_{-0.23}$	…
C_F		$0.65^{+0.07}_{-0.20}$	…	…
cos(θ_i)		<0.40	…	…
θ_i		…	…	<49.45
CTKcover		…	…	<0.16
TORσ		…	…	$21.27^{+5.99}_{-5.84}$
$A_{S,90}$		…	$0.23^{+0.11}_{-0.07}$	…
$A_{S,0}$		…	$3.49^{+1.68}_{-1.33}$	…
F_s($\times 10^{-3}$)		$6.03^{+1.72}_{-1.59}$	<4.14	$5.84^{+37.76}_{-2.06}$
Norm (10^{-3})		$1.72^{+0.02}_{-0.27}$	$1.75^{+0.66}_{-0.39}$	$3.89^{+1.00}_{-0.77}$
C_{AGN}	XMM-Newton	$0.78^{+0.07}_{-0.07}$	$0.82^{+0.09}_{-0.07}$	$0.78^{+0.08}_{-0.09}$
	NuSTAR	1	1	1
	Chandra	$0.26^{+0.13}_{-0.08}$	$0.27^{+0.12}_{-0.08}$	$0.24^{+0.12}_{-0.08}$
$N_{H,los} \times 10^{22}$ cm^{-2}	XMM-Newton	$28.09^{+2.26}_{-0.98}$	$32.02^{+3.53}_{-2.94}$	$30.39^{+3.01}_{-3.06}$
	NuSTAR	$13.92^{+1.46}_{-1.22}$	$12.96^{+1.79}_{-1.67}$	$15.06^{+1.80}_{-1.38}$
	Chandra	$13.42^{+6.01}_{-4.22}$	$13.11^{+6.63}_{-4.46}$	$12.90^{+6.21}_{-4.11}$
log $L_{NuSTAR,2-10\ keV}$		$43.04^{+0.01}_{-0.02}$	$42.92^{+0.08}_{-0.07}$	43.32
log $L_{NuSTAR,10-40\ keV}$		$43.38^{+0.01}_{-0.03}$	$42.76^{+0.14}_{-0.10}$	43.51
Red stat - No Var.		2.38	2.34	2.34
T		33.39	33.36	33.54
Red stat - No C_{AGN}Var.		1.00	0.97	1.01
T		0.13	0.63	0.30
Red stat - No $N_{H,los}$ Var.		1.14	1.14	1.12
T		3.82	3.57	3.07

Note. Same as Table 2.

Table 16
X-Ray Fitting Results for LEDA 2816387

Parameter		borus02	MYTorus dec	UXCLUMPY
χ^2/d.o.f		344.97/305	346.23/312	345.28/313
red χ^2		1.13	1.11	1.10
T		2.29	1.93	1.82
p-value		0.42	0.15	1
kT		$0.90^{+0.12}_{-0.11}$	$0.90^{+0.12}_{-0.11}$	$0.89^{+0.13}_{-0.13}$
apec norm($\times 10^{-6}$)		$6.60^{+2.08}_{-1.89}$	$6.59^{+1.90}_{-1.59}$	$5.51^{+1.87}_{-1.63}$
Γ		<1.4	<1.4	1.4^{*}
$N_{H,av} \times 10^{24}$ cm^{-2}		$0.05^{+0.03}_{-0.03}$	$0.09^{+0.14}_{-0.05}$	…
C_F		$0.25^{+0.19}_{-0.08}$	…	…
$\cos(\theta_i)$		<0.05	…	…
θ_i		…	…	90^{*}
CTKcover		…	…	<0.27
TORσ		…	…	$7.03^{+6.36}_{-2.23}$
$A_{S,90}$		…	$0.22^{+1.66}_{-0.15}$	…
$A_{S,0}$		…	$0.34^{+0.95}_{-0.4}$	…
$F_s(\times 10^{-3})$		$5.72^{+4.59}_{-2.82}$	$5.13^{+5.13}_{-3.22}$	$15.48^{+13.96}_{-9.07}$
Norm (10^{-3})		$1.08^{+0.03}_{-0.12}$	$1.16^{+0.03}_{-0.13}$	$1.34^{+0.41}_{-0.17}$
C_{AGN}	NuSTAR - 1	1	1	1
	XMM-Newton	$1.43^{+0.30}_{-0.16}$	$1.19^{+0.22}_{-0.08}$	$0.91^{+0.32}_{-0.26}$
	NuSTAR - 2	$0.98^{+0.21}_{-0.17}$	$0.99^{+0.20}_{-0.16}$	$0.98^{+0.18}_{-0.15}$
$N_{H,los} \times 10^{22}$ cm^{-2}	NuSTAR - 1	$66.55^{+7.71}_{-7.04}$	$64.28^{+7.55}_{-7.07}$	$62.97^{+7.37}_{-7.90}$
	XMM-Newton	$89.55^{+12.37}_{-10.15}$	$97.41^{+13.59}_{-9.57}$	$75.42^{+13.48}_{-11.68}$
	NuSTAR - 2	$76.32^{+10.75}_{-9.73}$	$75.46^{+10.41}_{-8.98}$	$73.98^{+9.12}_{-8.66}$
log $L_{NuSTAR,2-10\ keV}$		$44.28^{+0.01}_{-0.09}$	$44.26^{+0.02}_{-0.05}$	44.38
log $L_{NuSTAR,10-40\ keV}$		$44.58^{+0.05}_{-0.05}$	$44.57^{+0.05}_{-0.05}$	44.68
Red stat - No Var.		1.29	1.26	1.24
T		5.08	4.66	4.26
Red stat - No C_{AGN}Var.		1.14	1.24	1.10
T		2.42	4.20	1.73
Red stat - No $N_{H,los}$ Var.		1.15	1.17	1.11
T		2.62	3.02	1.91

Note. Same as Table 2. $\theta_{i,uxclumpy} = \arccos(\cos(\theta_{i,borus02}))$.

Appendix B
Source Spectra

In this section, we present the multiepoch best-fit spectra of the sources analyzed in this work, displayed in Figures 6 and 7, as modeled by borus02. We chose to show only borus02 best-fit spectra for clarity purposes. The spectra should be read as follows:

1. Considering we are simultaneously fitting all the observations available for a single source, all the observations for a single source are shown together, each with a different color.
2. All detectors in the same telescope are colored the same for each observation.
3. NuSTAR observations are colored chronologically, as listed in Table 1. The color order is as follows, from the first to the last: blue, green.
4. Chandra observations are colored chronologically, as listed in Table 1. The color order is as follows, from the first to the last: cyan, red.
5. Suzaku observations are colored chronologically, as listed in Table 1. The color order is as follows, from the first to the last: magenta, yellow.
6. XMM-Newton observations are colored chronologically, as listed in Table 1. The color order is as follows, from the first to the last: gray, orange.
7. A solid black line highlights the model's best fit for each observation.
8. The model components have the same color as the observation to which they correspond but different line styles. Reflection: dashed; Line-of-sight: dashed–dotted; Scattering: dashed–dotted-dot-dot; apec: dotted.

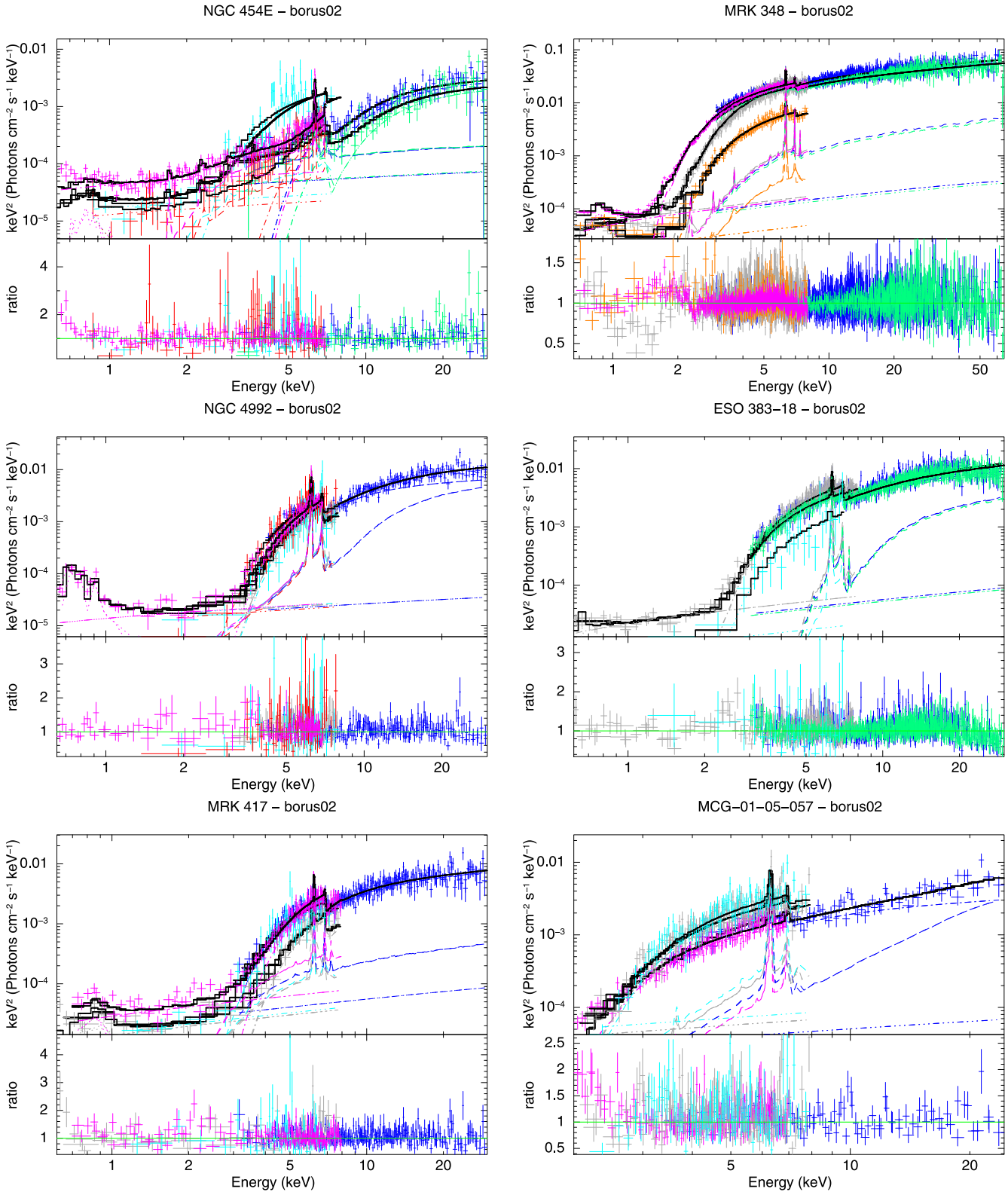

Figure 6. From left- to right-hand, top to bottom, unfolded `borus02` spectra of NGC 454e, MRK 348, NGC 4992, ESO 383-18, MRK 417, and MCG-01-05-027, respectively. Color code as explained in Appendix B.

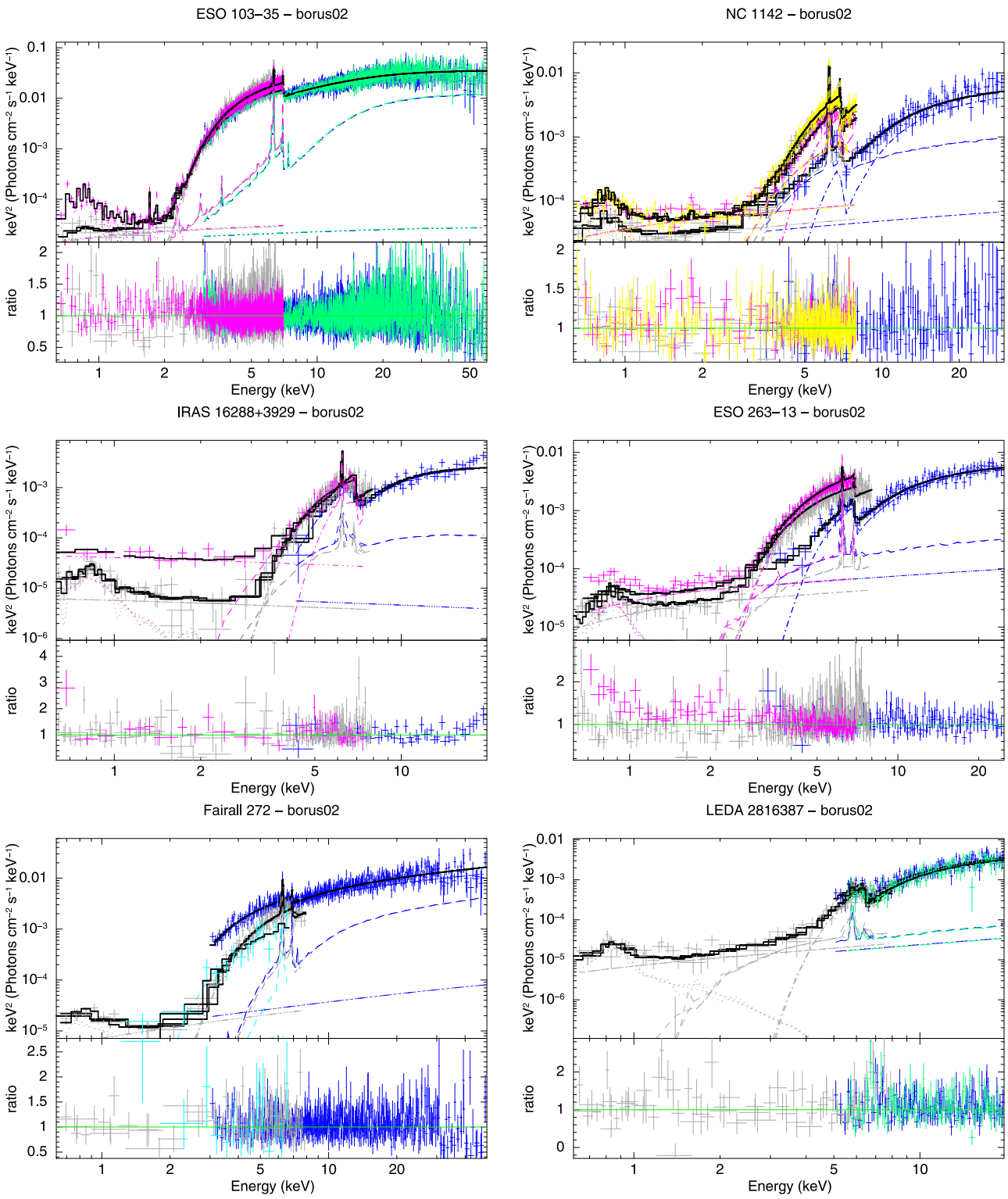

Figure 7. From left- to right-hand, top to bottom, unfolded `borus02` spectra of ESO 103-35, NGC 1142, IRAS 16288+3929, ESO 263-13, Fairall 272, and LEDA 2816387, respectively. Color code as explained in Appendix B.

Appendix C
$N_{H,los}$ Variability Plots

This appendix presents the line-of-sight hydrogen column density variability plots of the sources analyzed in this study, displayed in Figures 8 and 9.

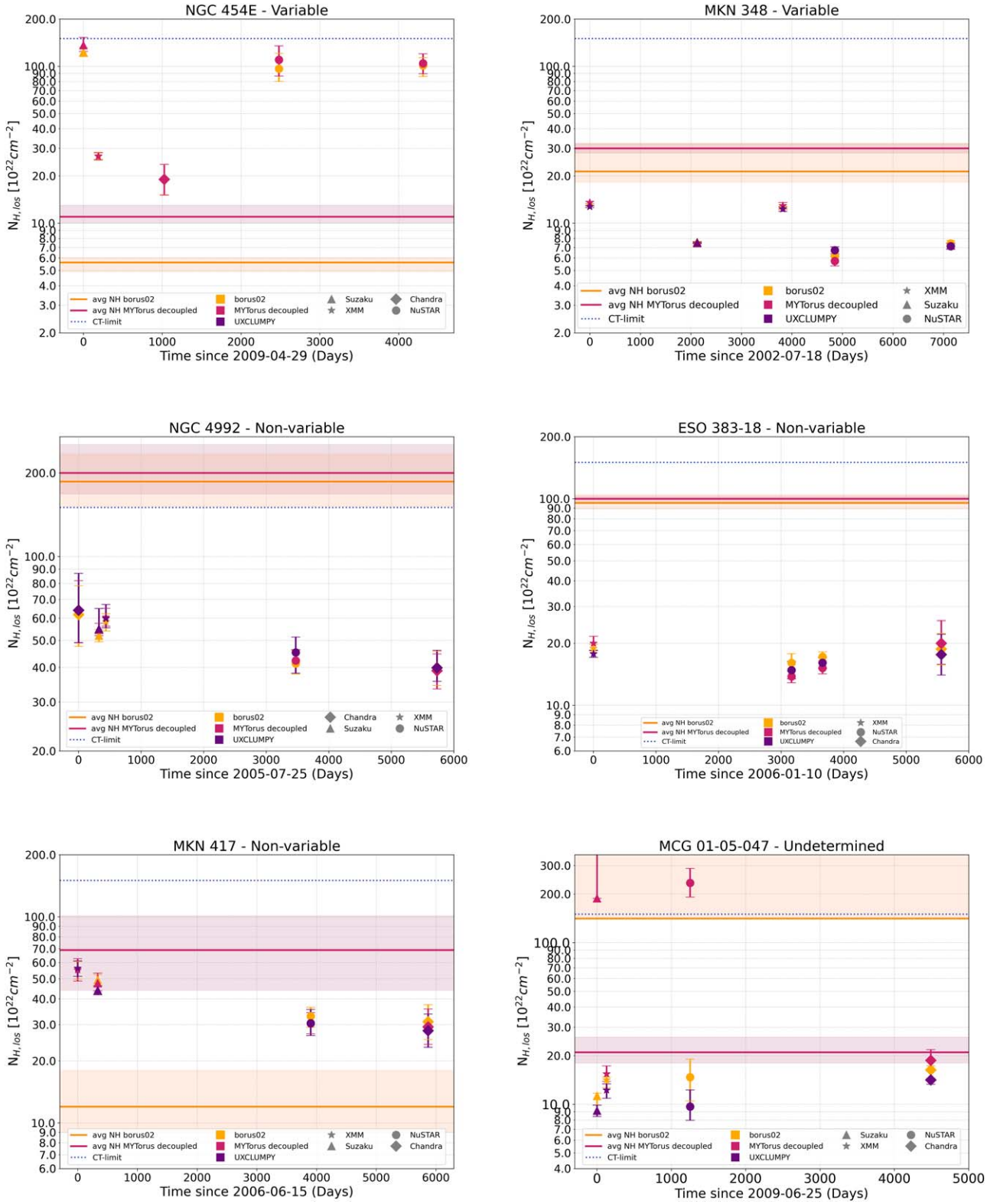

Figure 8. From left- to right-hand, top to bottom, line-of-sight hydrogen column density variability of NGC 454E, MRK 348, NGC 4992, ESO 383-18, MRK 417, and MCG-01-05-047, respectively. Color code as explained in Figure 2.

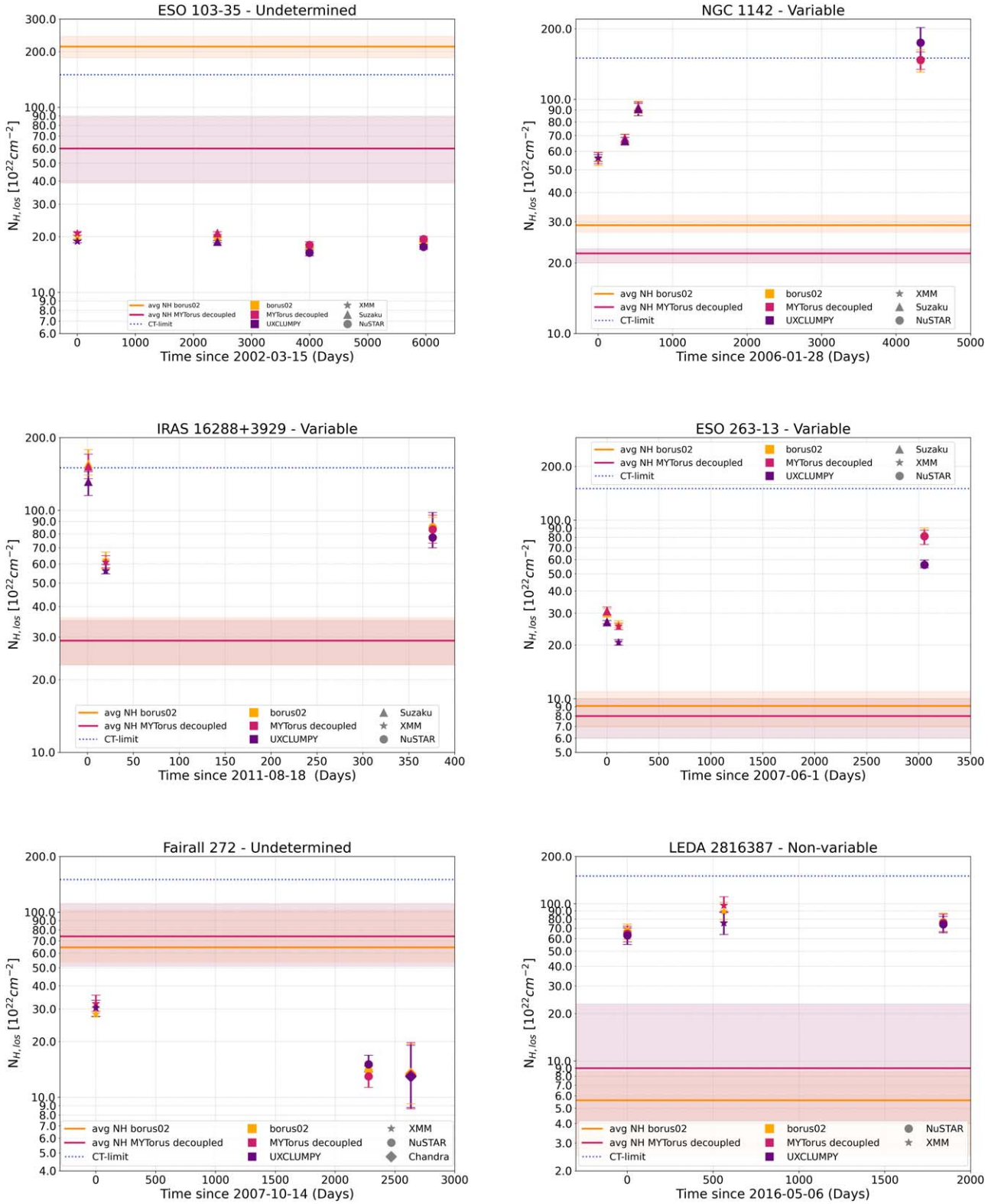

Figure 9. From left- to right-hand, top to bottom, line-of-sight hydrogen column density variability of ESO 103-35, NGC 1142, IRAS 16288+3929, Fairall 272, LEDA 2816387, and ESO 263-13, respectively. Color code as explained in Figure 2.

Appendix D
Comments on Individual Sources

In this appendix, we provide the specifics of data reduction and fitting procedures for each source when deviating from those outlined in Section 3. We comment on the results of the X-ray analysis for each individual source examined in the work, focusing on the contrast between the different models used. The comparison with the results obtained by XZ21 and other relevant works is also discussed.

D.1. NGC 454E

Data reduction and fitting: For the two Chandra observations, the background was extracted from a 15" circle in a uniform region to avoid contamination from a small emitting source located 10" from the nucleus. This second source is neither resolved by XMM-Newton nor Suzaku. Due to the data quality of the two Chandra observations, the spectra were binned with 5 and 3 cts bin^{-1}, respectively, applying C-statistics to the fit. Thus, we used a combination of χ^2 and C-stat as total statistics. Analysis of the results: NGC 454E is part of a merging system with the companion NGC 454W. As reported in E. Marchese et al. (2012), no X-ray emission is detected in the latter. We note that two observations, NuSTAR2 and Chandra 2, were taken almost simultaneously ($\Delta t = 6$ hr). After checking for possible intrinsic flux and luminosity variability, we opted to couple them in the spectral analysis. Thus, we consider them to be a unique joint observation. Due to the complexity of the six spectra analyzed in this work, as seen in the top left-hand panel of Figure 6, we only present results for `borus02` and `MYTorus` because `UXCLUMPY` failed to provide physically meaningful results. `MYTorus` and `borus02` are in good agreement, matching the results obtained by E. Marchese et al. (2012), whose analysis was performed only taking into account Suzaku, XMM-Newton, and Swift-XRT observations. XZ21 analysis, performed by modeling with `borus02` the first NuSTAR and the one XMM-Newton observations, found a thicker ($\gtrsim 10^{24}$ cm^{-2}) average torus density with respect to the one measured by our analysis, in which the $N_{H,av}$ is of the order of $\sim 10^{22}$ cm^{-2} for `borus02`, and $\sim 10^{23}$ cm^{-2} for `MYTorus`. We measure a $\Delta N_{H,los} \simeq 95 \times 10^{22}$ cm^{-2} over a time span of 190 days (~ six months), which would position the origin of the obscuration around ~90 pc from the central engine, following the approach first proposed by G. Risaliti et al. (2005). We note that for `borus02` the tension is above 3; however, when removing the variability from the analysis, we get much higher tensions ($T > 20$) in favor of the "$N_{H,los}$ Variable" scenario. This is also supported by the very low derived p-values. We thus classify the source as "$N_{H,los}$ Variable," in agreement with the variable nature of the source found by E. Marchese et al. (2012) and XZ21.

D.2. MRK 348

Data reduction and fitting: Chandra observation (ObsID: 12809) was not included in the fitting due to pile-up affecting the spectrum. The data quality of all of the observations was good enough to bin each spectrum with at least 15 cts bin^{-1}; we thus applied the χ^2 statistics to our data. Analysis of the results: The data are well fitted by all models, although we find a significant tension ($T > 10$) in all cases. This may be due to the large number of counts available for this source, suggesting that the models we use are too simple to fit the data. Nevertheless, there are no apparent issues observed in the fit residuals that might indicate specific problems. The best-fit data for the torus parameters and the $N_{H,los}$ are in good agreement between the three models, within errors. To properly model the soft part of the spectrum, we disentangled the `apec` normalization between the three soft observations (two XMM-Newton and one Suzaku). We froze `UXCLUMPY` inclination angle to be equal to the one we found using `borus02`, such that $\theta_{i,\mathrm{uxclumpy}} = \arccos(cos\theta_{i,\mathrm{borus02}}) = 70°$. Despite all the calculated tensions being $T > 10$, the "$N_{H,los}$ Variable" scenario is the one for which we find the lowest tension values. Considering this and the very low derived p-values, we classify this source as "$N_{H,los}$ Variable." The best-fit results are compatible with the ones found by XZ21 and E. Marchese et al. (2014). Both the aforementioned studies found variability in the absorber of MRK 348, in agreement with our classification of the AGN as "$N_{H,los}$ Variable."

D.3. NGC 4992

Data reduction and fitting: Due to the high particle background, we ignored the 0–3 keV and 0–4 keV range for XMM-*Newton* (ObsID 0312192101) and NuSTAR (ObsID 60061239002) spectra, respectively. We fit Chandra observations 1 and 2 applying C-statistics because the data quality forced us to bin them with 2 and 5 cts bin^{-1}, respectively. Thus, we used a combination of χ^2 and C-statistics as total statistics to fit the data. Analysis of the results: All models fit the data well and are in agreement with each other. We note that our results agree with the ones found by XZ21, although the latter found a slightly lower photon index with respect to the one measured in this work. We notice that although the hydrogen column density in the line of sight is Compton-thin ($\sim 10^{23}$ cm^{-2}), the average column density of the torus is CT ($>1.5 \times 10^{24}$ cm^{-2}). This is measured both by `borus02` and `MYTorus` and it is validated by the need of the CT inner ring in `UXCLUMPY` (CTKcover ~0.30), in a scenario similar to the one found by A. Pizzetti et al. (2022) for NGC 7479 and by NTA23 for NGC 612 and IC 4518A. The introduction of $N_{H,los}$ variability is unnecessary to fit the data well, reinforced by a p-value of > 0.01 for all models. We thus classify the source as 'Nonvariable in $N_{H,los}$'

D.4. ESO 383-18

Data reduction and fitting: Due to the poor data quality, we grouped the Chandra observation with 3 cts/bin, using C-statistic to fit the data. We thus use a mix of C-stat and χ^2 as total statistics. Analysis of the results: The data are well fitted by all models, although they do not strongly agree regarding general torus properties. `MYTorus` favors a face-on scenario, while `borus02` and `UXCLUMPY` favor an edge-on scenario, with a lower plasma temperature and photon index with respect to `MYTorus`, in agreement with what was found by XZ21. Within errors, the three models agree in the $N_{H,los}$ measurements and in the classification of the source as "Nonvariable in $N_{H,los}$"; we thus classify it as such.

D.5. MRK 417

Data reduction and fitting: Due to the low exposure time of the Chandra observation, we grouped the data with 5 cts bin^{-1} and used C-statistic for the fit. Analysis of the results: The three models fit the data well. However, `MYTorus` and `borus02` disagree on the $N_{H,av}$ determination, with `UXCLUMPY` favoring a transmission-dominated scenario (CTK = 0) rather than a reflection-dominated one as inferred by `borus02`, in accordance with what was found by XZ21. Nevertheless, the three models agree on the $N_{H,los}$ measurements. We cannot strongly affirm that $N_{H,los}$ variability is needed to fit the data, while the statistic analysis suggests flux variability is needed. We thus classify MRK 417 as "Nonvariable in $N_{H,los}$."

D.6. MCG-01-05-047

Data reduction and fitting: We omitted the energy range below 2 keV due to the complexity of the fitting procedure; thus, the fitting is performed in the 2–25 keV range. Analysis of the results: The three models disagree, with MYTorus fitting the data with a better statistic than borus02 and UXCLUMPY. While the first model favors a Compton-thin $N_{H,av}$ and a $N_{H,los}$-variable scenario, the latter models support a CT torus, in agreement with XZ21, with nonvariable Compton-thin clouds, wherein variability primarily arises from intrinsic flux fluctuations. We classify this source as "Undetermined" due to the models' disagreement in discerning the cause of variability.

D.7. ESO 103-35

Data reduction and fitting: We disentangled the apec normalization of the two soft X-ray observations to properly fit the soft part of the spectrum. Analysis of the results: The data are well fitted by the models. Both borus02 and UXCLUMPY support a reflection-dominated scenario, in which a high $N_{H,av}$ is needed to model the hard-energy tail of the data, in agreement with what reported by XZ21. MYTorus on the other hand, prefers a low $N_{H,av}$ and low scattering fraction scenario, although the photon index is in agreement with the other two models. As reported by J. A. Braatz et al. (1996) and mentioned in Section 5.2.3, ESO 103-35 hosts a nuclear 22 GHz water megamaser emission, which aligns in inclination with the torus: $\theta_{i,\mathrm{maser}} = 67^{\circ}$ (N. Bennert et al. 2004), $\theta_{i,\mathrm{torus}} \in [60^{\circ}–79^{\circ}.81]$. All models require intrinsic flux variability to fit the data, while only borus02 and UXCLUMPY favor a $N_{H,los}$-variable scenario. Additionally, the p-value is above the threshold for all three models, suggesting that the introduction of $N_{H,los}$ variability is not necessary to reach a proper fit. Although the results convey that some sort of variability is needed (either intrinsic flux or $N_{H,los}$), considering the discrepancy between the results, we classify this source as "Undetermined" because we are not able to discern the cause of such variability.

D.8. NGC 1142

Data reduction and fitting: No issues to report. Analysis of the results: The three models fit the data well and agree with each other. Although MYTorus and borus02 predict the average density of the torus to be Compton-thin, in agreement with what was found by XZ21, UXCLUMPY requires the additional thick inner ring to model the reflection component fully. Nevertheless, the three models fully agree with the measurements of the $N_{H,los}$. Interestingly, we measure a $\Delta N_{H,los} \simeq 25 \times 10^{22}\,\mathrm{cm}^{-2}$ between the two subsequent Suzaku observations, over a time span of ~ six months. This suggests the origin of the obscuration to be between ~1 and 49 pc from the central engine. The $N_{H,los}$ variable nature of this galaxy is also shown by the low tension and p-values derived by the statistical analysis, in agreement with XZ21; we thus classify NGC 1142 as "$N_{H,los}$ Variable."

D.9. IRAS 16288+3929

Data reduction and fitting: No issues to report. Analysis of the results: MYTorus and borus02 fit the data well, while UXCLUMPY shows poorer statistics. We note that the two former models favor a Compton-thin average torus density, in agreement with XZ21, while UXCLUMPY requires the addition of a geometrically thick (CTKcover > 0.57) CT reflector. Noticeably, IRAS 16288+3929 hosts a water megamaser, as reported by P. Castangia et al. (2013), suggesting the possible connection between the thick inner reflector predicted by UXCLUMPY and the warped megamaser disk (see, e.g., A. Masini et al. 2016; J. Buchner et al. 2021). The statistical analysis and the p-value derivation point toward a $N_{H,los}$-variable scenario; we then classify the source as such.

D.10. ESO 263-13

Data reduction and fitting: No issues to report. Analysis of the results: The three models are in agreement with each other, with UXCLUMPY showing slightly better statistics than the other two models. Although MYTorus and borus02 measure a Compton-thin $N_{H,av}$ ($\simeq 8 \times 10^{22}\,\mathrm{cm}^{-2}$), in agreement with the results obtained by XZ21, UXCLUMPY suggests the presence of a thick reflector to model the hard X-ray part of the spectrum. Both borus02 and UXCLUMPY favor a geometrically thin torus, in disagreement with the high covering factor ($C_F > 0.30$) found by XZ21. On the other hand, the models agree with XZ21 on the torus inclination angle, which is $\theta_i \gtrsim 40$. Despite no model yielding a $T < 3$, introducing both $N_{H,los}$ and flux variability is the scenario for which we derive the lowest tensions ($T_{\text{best-fit}} =$ 4.33–6.77, $T_{\text{No-var}} = 92.43$–$94.31$). Thus, also considering the very low derived p-values, we classify the source as "$N_{H,los}$ Variable."

D.11. Fairall 272

Data reduction and fitting: Due to the very low Chandra exposure time (2.9 ks), we bin the data to a minimum of 5 cts/bin, applying C-statistics; we then used a mix of χ^2 and C-statistics to the total fit. Analysis of the results: The three models slightly overfit the data, being in good agreement with each other. UXCLUMPY requires a geometrically thin (CTKcover < 0.16) CT reflector to fit the reflection hump, while MYTorus and borus02 find the overall torus density to be to the order of $\sim 7 \times 10^{23}\,\mathrm{cm}^{-2}$, in disagreement with the CT torus ($N_{H,av} \sim 10^{23}\,\mathrm{cm}^{-2}$) reported by XZ21. We note that all three models yield a p-value below the threshold, while the analysis of the tensions cannot discern the source of variability needed to model the data. We classify the source as "Undetermined."

D.12. LEDA 2816387

Data reduction and fitting: No issues to report. Analysis of the results: There is good agreement between the results of the three models, with UXCLUMPY yielding slightly better statistics. The three models find a hard photon index ($\Gamma < 1.4$), in agreement with what was found by XZ21. Both borus02 and MYTorus measure the $N_{H,av}$ to be Compton-thin, while UXCLUMPY seems to favor the presence of a denser component (CTKcover < 0.27). In addition, both UXCLUMPY and borus02 favor the edge-on scenario. The p-value is above the threshold for all the models, and the tensions are below 3 in both the variable and nonvariable case, leading us to classify the source as "Nonvariable in $N_{H,los}$."

D.13. 2MASX J06411806+3249313

Data reduction and fitting: For the XMM-Newton observation, MOS1 was not used because it was corrupted. Analysis of the results: We opted not to include apec in the analysis due to the low signal below 2 keV. The three models slightly overfit the

data but are overall in good agreement. Within errors, MYTorus and borus02 are in agreement with the $N_{H,av}$ measure obtained by XZ21, although UXCLUMPY requires a thicker reflector to model the hard X-ray part of the spectrum. Both borus02 and UXCLUMPY favor a face-on scenario, as also reported by XZ21. We also notice how the best-fit $N_{H,los}$ values are in the same range as $N_{H,av}$, in a scenario similar to the one reported by NTA23 for 3C 105, NGC 833, and NGC 612. Both the *p*-value and the tension analysis indicate a "Nonvariable in $N_{H,los}$" scenario, and we classify the source as such.

D.14. NGC 7479

Data reduction and fitting: Refer to A. Pizzetti et al. (2022) for details about the data reduction and fitting process. Analysis of the results: The three models agree in the classification of NGC 7479 as "Nonvariable in $N_{H,los}$," yielding a *p*-value above the threshold and tensions above 3.

D.15. NGC 6300

Data reduction and fitting: Refer to D. Sengupta et al. (2024) for details about the data reduction and fitting process. Analysis of the results: The three models used to analyze this source are borus02, UXCLUMPY, and XClumpy(A. Tanimoto et al. 2019). All of them slightly overfit the data but are in good agreement with each other. The *p*-value and tension analyses show that this is a variable source, but "Nonvariable in $N_{H,los}$." However, a *p*-value analysis of flux shows an indication of flux variability.

ORCID iDs

A. Pizzetti https://orcid.org/0000-0001-6412-2312
N. Torres-Albà https://orcid.org/0000-0003-3638-8943
S. Marchesi https://orcid.org/0000-0001-5544-0749
J. Buchner https://orcid.org/0000-0003-0426-6634
I. Cox https://orcid.org/0000-0003-2287-0325
X. Zhao https://orcid.org/0000-0002-7791-3671
D. Sengupta https://orcid.org/0009-0002-6991-1534
R. Silver https://orcid.org/0000-0001-6564-0517
M. Ajello https://orcid.org/0000-0002-6584-1703

References

Andonie, C., Bauer, F. E., Carraro, R., et al. 2022, A&A, 664, A46
Andrae, R., Schulze-Hartung, T., & Melchior, P. 2010, arXiv:1012.3754
Antonucci, R. 1993, ARA&A, 31, 473
Arnaud, K. A. 1996, in ASP Conf. Ser. 101, Astronomical Data Analysis Software and Systems V, ed. G. H. Jacoby & J. Barnes (San Francisco, CA: ASP), 17
Baloković, M., Brightman, M., Harrison, F. A., et al. 2018, ApJ, 854, 42
Baloković, M., Harrison, F. A., Madejski, G., et al. 2020, ApJ, 905, 41
Barthelmy, S. D., Barbier, L. M., Cummings, J. R., et al. 2005, SSRv, 120, 143
Bennert, N., Schulz, H., & Henkel, C. 2004, A&A, 419, 127
Bennett, C. L., Larson, D., Weiland, J. L., & Hinshaw, G. 2014, ApJ, 794, 135
Bianchi, S., Guainazzi, M., Matt, G., et al. 2005, A&A, 442, 185
Boorman, P. G., Torres-Albà, N., Annuar, A., et al. 2024, FrASS, 11, 1335459
Braatz, J. A., & Gugliucci, N. E. 2008, ApJ, 678, 96
Braatz, J. A., Henkel, C., Greenhill, L. J., Moran, J. M., & Wilson, A. S. 2004, ApJL, 617, L29
Braatz, J. A., Wilson, A. S., & Henkel, C. 1996, ApJS, 106, 51
Buchner, J., & Bauer, F. E. 2017, MNRAS, 465, 4348
Buchner, J., Brightman, M., Baloković, M., et al. 2021, A&A, 651, A58
Buchner, J., Brightman, M., Nandra, K., Nikutta, R., & Bauer, F. E. 2019, A&A, 629, A16
Buchner, J., Brightman, M., Nandra, K., Nikutta, R., & Bauer, F. E. 2019, A&A, 629, A16
Castangia, P., Panessa, F., Henkel, C., Kadler, M., & Tarchi, A. 2013, MNRAS, 436, 3388
Comastri, A. 2004, in Astrophysics and Space Science Library, Vol. 308, Supermassive Black Holes in the Distant Universe, ed. A. J. Barger (Dordrecht: Kluwer), 245
Combes, F., Garcìa-Burillo, S., Audibert, A., et al. 2019, A&A, 623, A79
Fruscione, A., McDowell, J. C., Allen, G. E., et al. 2006, Proc. SPIE, 6270, 62701V
Furui, S., Fukazawa, Y., Odaka, H., et al. 2016, ApJ, 818, 164
Gabriel, C., Denby, M., Fyfe, D. J., et al. 2004, in ASP Conf. Ser. 314, Astronomical Data Analysis Software and Systems (ADASS) XIII, ed. F. Ochsenbein, M. G. Allen, & D. Egret (San Francisco, CA: ASP), 759
Garcìa-Burillo, S., Alonso-Herrero, A., Ramos Almeida, C., et al. 2021, A&A, 652, A98
Gianolli, V. E., Kim, D. E., Bianchi, S., et al. 2023, MNRAS, 523, 4468
Greenhill, L. J., Booth, R. S., Ellingsen, S. P., et al. 2003a, ApJ, 590, 162
Greenhill, L. J., Kondratko, P. T., Lovell, J. E. J., et al. 2003b, ApJL, 582, L11
Greenhill, L. J., Kondratko, P. T., Moran, J. M., & Tilak, A. 2009, ApJ, 707, 787
Greenhill, L. J., Tilak, A., & Madejski, G. 2008, ApJL, 686, L13
Haardt, F., Maraschi, L., & Ghisellini, G. 1994, ApJl, 432, L95
Hernández-Garcìa, L., Masegosa, J., González-Martìn, O., & Márquez, I. 2015, A&A, 579, A90
Herrnstein, J. R., Moran, J. M., Greenhill, L. J., & Trotter, A. S. 2005, ApJ, 629, 719
Hönig, S. F. 2019, ApJ, 884, 171
Jansen, F., Lumb, D., Altieri, B., et al. 2001, A&A, 365, L1
Kalberla, P. M. W., Burton, W. B., Hartmann, D., et al. 2005, A&A, 440, 775
Koss, M. J., Ricci, M. J., Trakhtenbrot, C., et al. 2022, ApJS, 261, 2
Kuo, C. Y., Braatz, J. A., Condon, J. J., et al. 2011, ApJ, 727, 20
Laha, S., Markowitz, A. G., Krumpe, M., et al. 2020, ApJ, 897, 66
Lawrence, A., & Elvis, M. 2010, ApJ, 714, 561
Marchese, E., Braito, V., Della Ceca, R., Caccianiga, A., & Severgnini, P. 2012, MNRAS, 421, 1803
Marchese, E., Braito, V., Reeves, J. N., et al. 2014, MNRAS, 437, 2806
Marchesi, S., Zhao, X., Torres-Albà, N., et al. 2022, ApJ, 935, 114
Markowitz, A. G., Krumpe, M., & Nikutta, R. 2014, MNRAS, 439, 1403
Masini, A., Comastri, A., Baloković, M., et al. 2016, A&A, 589, A59
Murphy, K. D., & Yaqoob, T. 2009, MNRAS, 397, 1549
Nenkova, M., Sirocky, M. M., Ivezić, Ž., & Elitzur, M. 2008a, ApJ, 685, 147
Nenkova, M., Sirocky, M. M., Nikutta, R., Ivezić, Ž., & Elitzur, M. 2008b, ApJ, 685, 160
Oh, K., Koss, M., Markwardt, C. B., et al. 2018, ApJS, 235, 4
Panessa, F., & Giroletti, M. 2013, MNRAS, 432, 1138
Peck, A. B., Henkel, C., Ulvestad, J. S., et al. 2003, ApJ, 590, 149
Petterson, J. A. 1977, ApJ, 214, 550
Pizzetti, A., Torres-Albà, N., Marchesi, S., et al. 2022, ApJ, 936, 149
Ramos Almeida, C., & Ricci, C. 2017, NatAs, 1, 679
Risaliti, G., Elvis, M., Fabbiano, G., Baldi, A., & Zezas, A. 2005, ApJL, 623, L93
Risaliti, G., Elvis, M., Fabbiano, G., et al. 2007, ApJL, 659, L111
Risaliti, G., Elvis, M., & Nicastro, F. 2002, ApJ, 571, 234
Ross, R. R. 1979, ApJ, 233, 334
Sanfrutos, M., Miniutti, G., Agìs-González, B., et al. 2013, MNRAS, 436, 1588
Schartmann, M., Meisenheimer, K., Camenzind, M., Wolf, S., & Henning, T. 2005, A&A, 437 , 861, 20042363
Sengupta, D., Torres-Albà, N., Pizzetti, A., et al. 2024, arXiv:2410.02878
Serafinelli, R., Braito, V., Reeves, J. N., et al. 2023, A&A, 672, A10
Siebenmorgen, R., Heymann, F., & Efstathiou, A. 2015, A&A, 583, A120
Simpson, C. 2005, MNRAS, 360, 565
Smith, R. K., Brickhouse, N. S., Liedahl, D. A., & Raymond, J. C. 2001, ApJL, 556, L91
Stalevski, M., Fritz, J., Baes, M., Nakos, T., & Popović, L. Č. 2011, BaltA, 20, 490
Stephens, M. A. 1974, JASA, 69, 730
Tanimoto, A., Ueda, Y., Odaka, H., et al. 2019, ApJ, 877, 95
Torres-Albà, N., Marchesi, S., Zhao, X., et al. 2023, A&A, 678, A154
Torres-Albà, N., Iwasawa, K., Dìaz-Santos, T., et al. 2018, A&A, 620, A140
Urry, C. M., & Padovani, P. 1995, PASP, 107, 803
Vasudevan, R. V., Fabian, A. C., Gandhi, P., Winter, L. M., & Mushotzky, R. F. 2010, MNRAS, 402, 1081
Yaqoob, T. 2012, MNRAS, 423, 3360
Yaqoob, T., Tatum, M. M., Scholtes, A., Gottlieb, A., & Turner, T. J. 2015, MNRAS, 454, 973
Zhao, X., Marchesi, S., Ajello, M., et al. 2021, A&A, 650, A57